Doctorate of Philosophy

Schrödinger's Catwalk

Machine learning methods to distill models of quantum systems

Brian Flynn

University of Bristol

July, 2021

ABSTRACT

Quantum technologies exploit quantum mechanical processes to achieve outcomes beyond the reach of classical machinery. One of their most promising applications is quantum simulation, whereby particles, atoms and molecules can be examined thoroughly for the first time, having been beyond the scope of even the most powerful supercomputers.

Models have been useful tools in understanding physical systems: these are mathematical structures encoding physical interactions, which allow us to predict how the system will behave under various conditions. Models of quantum systems are particularly difficult to design and test, owing to the huge computational resources required to represent them accurately. In this thesis, we introduce and develop an algorithm to characterise quantum systems efficiently, by inferring a model consistent with their observed dynamics. The *Quantum Model Learning Agent* (QMLA) is an extensible framework which permits the study of any quantum system of interest, by combining quantum simulation with state of the art machine learning. QMLA iteratively proposes candidate models and trains them against the target system, finally declaring a single model as the best representation for the system of interest.

We describe QMLA and its implementation through open source software, before testing it under a series of physical scenarios. First, we consider idealised theoretical systems in simulation, verifying the core principles of QMLA. Next, we incorporate strategies for generating candidate models by exploiting the information QMLA has gathered to date; by incorporating a genetic algorithm within QMLA, we explore vast spaces of valid candidate models, with QMLA reliably identifying the precise target model. Finally, we apply QMLA to *realistic* quantum systems, including operating on experimental data measured from an electron spin in a nitrogen vacancy centre.

QMLA is shown to be effective in all cases studied in this thesis; however, of greater interest is the platform it provides for examining quantum systems. QMLA can aid engineers in configuring experimental setups, facilitate calibration of near term quantum devices, and ultimately enable complete characterisation of natural quantum structures. This thesis marks the beginning of a new line of research, into automating the understanding of quantum mechanical systems.

DECLARATION OF AUTHORSHIP

This dissertation is submitted to the University of Bristol in accordance with the requirements for award of the degree of Doctorate of Philosophy in the Faculty of Science.

I declare that the work in this dissertation was carried out in accordance with the requirements of the University's *Regulations and Code of Practice for Research Degree Programmes* and that it has not been submitted for any other academic award. Except where indicated by specific reference in the text, the work is the candidate's own work. Work done in collaboration with, or with the assistance of, others, is indicated as such. Any views expressed in the dissertation are those of the author.

Signed:

Date:

Word count: $\sim 50,000$

ACKNOWLEDGEMENTS

I was never one of those people destined for a PhD. I don't think I knew what a PhD was until half way through my undergraduate studies, by which time I was resigned to being tapped on the shoulder one day and asked to leave the campus, once they realised I had been faking it all along. So, at the risk of bragging, I am proud of this thesis, and the work it took to get here.

When you set out to write a thesis, you are constantly reminded that no one will ever *actually* read it, and you must therefore decide how much time and effort to spend on a document to gather dust on the electronic shelves of the university's digital library. I spent more time than most – not for the sake of examiners, supervisors or hypothetical future students, but for myself, as evidence that I can produce good work when I really try.

In the following 200 pages, I list in (sometimes boring) detail almost everything I've learned in the last four and a half years. I've learned something else important: the people around matter, and you need to tell them that once in a while. Here I just want to mention some people that have helped me along the way, or have been kind enough to share their time with me in some capacity. If the world is lucky, I will never again write anything this long, so I will have to write a lifetime worth of acknowledgements here. I will start in Bristol and work my way home.

The first person to thank has to be Raf, since this entire thesis builds on his initial idea. Beyond giving me the base material to work on for my PhD, he has also given me a huge amount of help and support over the last few years, along with friendship. His passion for machine learning is matched only by his passion for everything else; he is endlessly interested in all facets of science. I hope to live up to his example.

Andreas was equally crucial to any achievements I can claim. Through countless late night messages, he guided everything about this work that succeeded. Several times I thought I had outwitted him, and understood a concept more than him – until a few hours later when I realised I was wrong and he had explained it to me days before. Thanks for sticking with it.

To Anthony and the rest of the Laing gang (pronounced *Leng geng*), thanks for the wisdom, stories and beers. The wider *QETLabs* group is a real privilege to have been part of – it's been inspiring and terrifying to be surrounded by such talented people. Thanks to Sebastian for carefully reading my chapter on his beloved NV centres. Thanks to everyone involved for putting up with me.

The *Quantum Engineering Centre for Doctoral Training* gave me an opportunity I never thought I'd have, as well as a community to enjoy it with. The idea that I can call myself a scientist means a lot to me, and simply would not have happened if the QECDT hadn't taken a chance on me – I will always appreciate it. Of course, the CDT peaked with cohort 3: thanks to Dave for being willing to share a house in our first year, to Will for teaching me how to play squash (and beating me every time), and Max for a recent phone call where we agreed that thesis

acknowledgements should read like the acceptance speech to an *Oscar* you've awarded yourself, and to fully embrace it. I am grateful to Jorge (and Holly) for thinking of me to run *Quantum in the Summer* together, and to Konstantina for working most closely with me along the way.

I moved to Bristol for a PhD, but I surely wouldn't have stayed without building a good life here. I've enjoyed all the time spent cycling; playing Gaelic football, soccer and squash; learning mind games like Avalon, and trips to cinemas and restaurants with colleagues and friends. I always say – you can easily fill six nights per week with wholesome, healthy activities, without drinking. For the seventh night, however, you should hope to make friends like I did: Alex, Dom, Jake, Joel, Frazer, Reece, and all those mentioned already. Patrick had the unique punishment of thesis-reader, office-mate and pub-goer (I am not sure what past-life indiscretion he is atoning for, but I'm grateful for it as well). My happiest memories of this stage of my life will be sunny beer gardens on Friday afternoons with all of the above.

While the last year of my PhD (and thesis writing) coincided with Covid-19 lockdowns, one silver lining has been catching up online with my friends from Dublin more regularly. It is a pleasure to lose money to you all in poker, and I look forward to losing in person. Niall read my attempt to explain quantum mechanics, and was gracious enough not to berate me for it. James and John Mark put up with more than their fair share over a number of weekends. Evan has read every CV, paper, and now thesis, that I've written in the last eight years. If Roy Keane had for football the passion Evan has for physics, Ireland would have won the 2002 World Cup.

Weekends spent with old friends are high on my list of favourite things. I am always pleased when someone goes out of their way to visit – thanks to anyone who has gotten on a plane or train for my sake. Special mention to *Big Red* – a lifelong friend with a talent for meandering, all-encompassing conversation, and a unique outlook: I've heard many people say *Would this make me rich/famous/fulfilled*, you're the only one to ever ask *Would this make me happy?*

Along with all of the great people above, I am lucky to have a supportive family. I hope this thesis goes some way to answering your question, *what do you actually do?* To the next generation: I hope one day in ten or fifteen years, you will find this thesis some rainy afternoon. If you ask about it, don't believe them if they tell you I was smart. Believe them if they that say I worked hard, but that I thoroughly enjoyed it – it would not have been worth doing otherwise.

More important than any thesis, these years will be remembered for the short time we got to spend with Lola and Luca. I still don't have words elegant enough to lessen their loss – I just wanted to acknowledge them here.

To Mam and Dad, sincere thanks for everything. We know you're proud of us; we're proud of you too.

Finally, Emma has been constant across all aspects of my life. I don't deserve the patience you've shown, especially this last year when I've been even more stressful, but I will always appreciate it, and do my best to make it worth your while.

Go raibh míle maith agaibh,
Brian

For
Lola & Luca

CONTENTS

Abstract i
Declaration of Authorship ii
Acknowledgements iii
List of Tables viii
List of Figures ix
Acronyms xi
Glossary xiii
List of Publications xv

Introduction

I CONTEXTUAL REVIEW

II ALGORITHMS

III THEORETICAL STUDY

IV EXPERIMENTAL STUDIES

1 NITROGEN VACANCY CENTRE 6
1.1 Nitrogen-vacancy centre . . . 6
1.1.1 Experimental procedure . . . 9
1.2 Target system . . . 13
1.2.1 Mapping to model terms . . . 14
1.2.2 Prior knowledge . . . 16
1.3 Exploration strategy . . . 17
1.3.1 Test in simulation . . . 20
1.4 Experiment design constraints . . . 20
1.5 Results . . . 21
1.5.1 Analysis . . . 23
1.5.2 Finite size effects . . . 26
1.5.3 Outlook . . . 28
2 LARGER REALISTIC SYSTEMS 29
2.1 Target system . . . 29
2.2 Genetic algorithm . . . 32
2.2.1 Parameter learning . . . 32
2.2.2 Results . . . 33

V CONCLUSION
3 OUTLOOK FOR MODEL LEARNING METHODOLOGIES 38
Bibliography 40

LIST OF TABLES

Table 1.1 QMLA win rates and R^2 for models based on experimental data and simulations 23
Table 2.1 Terms permitted in the QMLA genetic algorithm when modelling the extended nitrogen-vacancy centre systems 31
Table 2.2 Percentage of instances for which each term is found by QMLA genetic algorithm studying nitrogen-vacancy centre system 36

LIST OF FIGURES

Figure 1.1 Nitrogen-vacancy centre energy levels 8
Figure 1.2 States of spin qubit at each stage of Hahn echo sequence shown on the Bloch sphere 10
Figure 1.3 Raw data for nitrogen-vacancy centre's dynamics 12
Figure 1.4 Greedy model search 18
Figure 1.5 QMLA applied to experimental nitrogen-vacancy centre system 22
Figure 1.6 Models considered by QMLA for simulated/experimental nitrogen-vacancy centre data, and their win rates 24
Figure 1.7 Dynamics reproduced by QMLA champion models for simulated/experimental data 25
Figure 1.8 Histograms for parameters learned by QMLA champion models on simulated and experimental data 27
Figure 1.9 Predicted revivals of QMLA champion model 28
Figure 2.1 Long-time dynamics for nitrogen-vacancy centres 30
Figure 2.2 Evaluation dataset for nitrogen-vacancy centre genetic algorithm 33
Figure 2.3 Instance of genetic algorithm for simulated nitrogen-vacancy centre system with four qubits 34
Figure 2.4 Nitrogen-vacancy centre genetic algorithm run 35
Figure 2.5 Hinton diagram of terms found for 4-qubit nitrogen-vacancy centre model 35

LISTINGS

ACRONYMS

C	carbon
^{14}N	nitrogen-14
AI	artificial intelligence
AIC	Akaike information criterion, **??**
AICC	Akaike information criterion corrected, **??**
BF	Bayes factor, **??**
BFEER	Bayes factor enhanced Elo ratings, **??**
BIC	Bayesian information criterion, **??**
CLE	classical likelihood estimation, **??**
CPU	central processing unit
DAG	directed acyclic graph
EDH	experiment design heuristic, **??**
ES	exploration strategy, **??**
ET	exploration tree, **??**
FH	Fermi-Hubbard
FN	false negatives, **??**
FP	false positives, **??**
GA	genetic algorithm, **??**
GES	genetic exploration strategy
GPU	graphics processing unit
IQLE	interactive quantum likelihood estimation, **??**
JWT	Jordan Wigner transformation, **??**
LE	Loschmidt echo, **??**
LTL	log total likelihood, **??**

ML machine learning, **??**
MW microwave

NV nitrogen-vacancy
NVC nitrogen-vacancy centre, Section 1.1

OF objective function, **??**

PBS portable batch system
PGH particle guess heuristic, **??**
PL photoluminescence

QC quantum computer, **??**
QHL quantum Hamiltonian learning, **??**.
QL quadratic loss, **??**
QLE quantum likelihood estimation, **??**
QM quantum mechanics, **??**
QML quantum machine learning, **??**
QMLA Quantum Model Learning Agent, **??**.

SMC sequential Monte Carlo, **??**

TL total likelihood, **??**
TLTL total log total likelihood, **??**
TN true negatives, **??**
TP true positives, **??**

VQE variational quantum eigensolver

GLOSSARY

N_E	Number of experiments to perform during model training through QHL.
N_P	Number of particles used when training a model through QHL.
Q	Quantum system which is the target of QMLA, i.e. the system to be characterised.
$\hat{H}_0$	True model for the target system, Q; i.e. the Hamiltonian model form which QMLA is attempting to retrieve in a given instance.
F_1-score	F_1-score, measure of model quality with respect to $\hat{H}_0$, $f \in [0, 1]$, **??**.
champion	See champion model.
champion model	The model deemed by QMLA as the most suitable for describing the target system.
chromosome	A single candidate, in the space of valid solutions to the posed problem in a genetic algorithm, **??**.
Elo rating	Points transfer system for quantifying relative ability of candidates in a competitive domain, modified for use as an objective function within the genetic algorithm of QMLA, **??**
expectation value	Average outcome expected by measuring an observable of a quantum system many times, **??**.
experiment	Experiment performed upon Q when training a model through QHL, **??**.
gene	Individual element within a chromosome.
Hamiltonian	Mathematical structure which captures all interactions to which a quantum system is subject, **??**.
hyperparameter	Variable within an algorithm that determines how the algorithm itself proceeds.
instance	A single implementation of the QMLA algorithm, resulting in a nominated champion model.
likelihood	Value that represents how likely a hypothesis is; usually used in the context of likelihood estiamation, **??**.

model The mathematical description of some quantum system, **??**.

model search Exploration through the model space performed by QMLA, where the progression of the search is determined by the ES **??**.

model space Abstract space containing all descriptions (within defined constraints such as dimension) of the system as models, **??**.

particle Sampled from prior distribution during model training through QHL, each particle gives a parameterisation corresponding to a unique hypothesis about Q, **??**.

probe Input state, $|\psi\rangle$, into which the target system is initialised, before unitary evolution, **??**.

results directory Directory to which the data and analysis for a given run of QMLA are stored.

run Collection of QMLA instances, usually targeting the same system with the same initial conditions.

spawn Process by which new models are generated within an ES, ususally by combining previously considered models.

success rate Fraction of instances within a run where QMLA nominates the true model as champion.

term Individual constituent of a model, e.g. a single operator within a sum of operators, which in total describe a Hamiltonian, **??**.

true model The model which correctly describes the target system. $\hat{H}_0$ is known for simulated Q but not known precisely for experimental systems.

volume Volume of a parameter distribution's credible region, **??**.

win rate The fraction of instances for which a given candidate model was nominated as champion within a run of QMLA.

LIST OF PUBLICATIONS

The work presented in this thesis has appeared[1] publicly in several formats.

Papers

1. *Learning models of quantum systems from experiments.* A.A. Gentile, Brian Flynn, S, Knauer, N. Wiebe, S. Paesani, C. E. Granade, J. G. Rarity, R. Santagati and A. Laing. arXiv preprint arXiv:2002.06169 (2020); accepted *Nature Physics* (2021); referred to throughout as [1].
2. *Quantum Model Learning Agent: quantum systems' characterisation through machine learning.* Brian Flynn, A.A. Gentile, R. Santagati, N. Wiebe and A. Laing. Reporting outcomes of studies on theoretical systems as described in this thesis. In Preparation (2021); referred to throughout as [2].
3. *Quantum Model Learning Agent: Python framework for characterising quantum systems.* Brian Flynn, A.A. Gentile, R. Santagati, N. Wiebe and A. Laing. Technical manuscript detailing software implementation. In Preparation (2021).

Software

4. *QMLA: Python framework for the reverse engineering of Hamiltonian models of quantum systems through machine learning.* Brian Flynn, A.A. Gentile, R. Santagati, N. Wiebe, S. Paesani, C. E. Granade, and A. Laing. Codebase; open sourced via Github repository; referrred to throughout as [3].
5. *Quantum Model Learning Agent*. Brian Flynn, A.A. Gentile, R. Santagati, N. Wiebe, S. Paesani, C. E. Granade, and A. Laing. Documentation for codebase; referrred to throughout as [4].

Conference Proceedings - Talks [2]

6. *Quantum Model Learning Agent.* Brian Flynn, A.A. Gentile, R. Santagati, S, Knauer, N. Wiebe, S. Paesani, C. E. Granade, J. G. Rarity, and A. Laing. Quantum Techniques in Machine Learning, Online, 2020.

1 Or will appear in the near future.
2 Note: only conferences proceedings presented by the author are included.

7. *Learning models of quantum systems from experiments.* Brian Flynn, A.A. Gentile, R. Santagati, S, Knauer, N. Wiebe, S. Paesani, C. E. Granade, J. G. Rarity, and A. Laing. Bristol Quantum Information Technologies, Online, 2020.
8. *Quantum Model Learning: characterizing quantum systems through machine learning*. Brian Flynn, A.A. Gentile, R. Santagati, S, Knauer, N. Wiebe, S. Paesani, C. E. Granade, J. G. Rarity, and A. Laing. Quantum Techniques in Machine Learning, Daejeon, South Korea, 2019.
9. *Quantum Model Learning Agent.* Brian Flynn, A.A. Gentile, R. Santagati, S, Knauer, N. Wiebe, S. Paesani, C. E. Granade, J. G. Rarity, and A. Laing. Quantum Engineering Centre for Doctoral Training Conference, Bristol, UK, 2019. Awarded *Talk prize*.

Conference Proceedings - Posters

10. *Quantum Model Learning Agent.* Brian Flynn, A.A. Gentile, R. Santagati, S, Knauer, N. Wiebe, S. Paesani, C. E. Granade, J. G. Rarity, and A. Laing. Machine Learning for Quantum, IOP Conference, Online, 2021. Awarded *Poster prize*.
11. *Quantum Model Learning.* Brian Flynn, A.A. Gentile, R. Santagati, S, Knauer, N. Wiebe, S. Paesani, C. E. Granade, J. G. Rarity, and A. Laing. Machine Learning for Quantum Technologies, Erlangen, Germany, 2019.
12. *Quantum Model Learning.* Brian Flynn, A.A. Gentile, R. Santagati, S, Knauer, N. Wiebe, S. Paesani, C. E. Granade, J. G. Rarity, and A. Laing. Bristol Quantum Information Technologies, Bristol, UK, 2019.
13. *Quantum Model Learning: characterizing quantum systems through machine learning.* Brian Flynn, A.A. Gentile, R. Santagati, S, Knauer, N. Wiebe, S. Paesani, C. E. Granade, J. G. Rarity, and A. Laing. Quantum Engineering Centre for Doctoral Training Conference, Bristol, UK, 2018. Awarded *Poster prize*.

INTRODUCTION

Part I

CONTEXTUAL REVIEW

Part II

ALGORITHMS

Part III

THEORETICAL STUDY

Part IV

EXPERIMENTAL STUDIES

1 NITROGEN VACANCY CENTRE

It is of primary interest to apply the Quantum Model Learning Agent (QMLA) algorithm to real-life, experimental systems. In this chapter we devise an exploration strategy (ES) to operate in conjunction with experimental data in order to characterise an electron spin in a nitrogen-vacancy centre (NVC) in diamond. In particular, we model, through Hamiltonian terms, interactions between the spin and the spin bath in which it resides, so that QMLA is finding an effective model for the open system dynamics.

Here we will first introduce a basic picture of NVCs, using basic but nonstandard nomenclature for simplicity; for thorough descriptions of the underlying physics, readers are referred to [5]. We next discuss the target system with respect to its modelling, determining the suitable terms which *might* represent the NVC's interactions, to inform the starting point for QMLA. Finally we describe the implementation of an ES for the examination of the NVC, and the results of the QMLA procedure.

1.1 NITROGEN-VACANCY CENTRE

Nitrogen vacancies are point defects in diamond, occuring intrinsically (naturally) [6] or extrinsically (synthetically) [7,8]. A substitutional nitrogen-14 (^{14}N) isotope is embedded in a lattice of carbon atoms in diamond, adjacent to a lattice vacancy, such that it is surrounded by three carbons (Cs) (either ^{12}C or ^{13}C) [9]. Of the ^{14}N atom's five valence electrons, three bond with nearby Cs; the remaining two unbonded electrons couple with the lattice vacancy, forming a triplet state, considered as the NVC. We can experimentally drive the outer electron, moving the NVC between energy levels characterised by the triplet. In this section we describe how we can exploit those energy levels in order to define a mechanism by which to prepare and implement gates on the controlled system, a readout procedure and a computational basis.

A *manifold* is a set of states with marginal differences, such as a single differing quanutm number. For example, states near the absolute ground state might differ only in their magnetic spin quantum number: together they can be characterised as the *ground state manifold*. We consider two principal manifolds of the system: the ground state and excited manifolds, each consisting of three states, corresponding to the allowed values for magnetic spin m_s, see Fig. 1.1a. For brevity, we denote states with reference to their magnetic spin and manifold, e.g. the state in the ground state manifold with $m_s = 0$ is denoted $|m_s = 0\rangle_g$. In the absence of a magnetic field, the states corresponding to $|m_s = \pm 1\rangle$ are degenerate, but in the presence of a magnetic field, B, they have distinct energy levels, referred to as the Zeeman effect, Fig. 1.1b.

For the purposes of computation, we choose the ground state and one of the excited states as the two levels of a qubit. We designate the states $|m_s = 0\rangle_g$ and $|m_s = -1\rangle_g$ as the computational

basis states $|0\rangle, |1\rangle$ respectively, such that we have defined a qubit and computational basis, Fig. 1.1d. We also require a reliable mechanism through which we can be confident that our qubit is in a definite state, to serve as the starting point of computation: usually qubits are initialised to $|0\rangle$, so here we aim to prepare the NVC in $|m_s = 0\rangle_g$. By shining a laser of 532 nm (green) on the NVC, irrespective of which state within the ground state manifold the spin starts, it is excited in to the excited manifold, from which it decays back to the ground state manifold. The process of this decay can be exploited for the preparation of the NVC in $|m_s = 0\rangle_g$ and therefore enable initialisation for computation. That is, when the NVC is excited to the $|m_s = 0\rangle_e$ level, the dominant decay process is spin-preserving, so after decay it ends in $|m_s = 0\rangle_g$. On the other hand, if the NVC had been excited instead to $|m_s = \pm 1\rangle_e$, the dominant decay process is through a meta-stable/shelving state, which does not preserve spin, so in this case it also ultimately decays to the $|m_s = 0\rangle_g$, Fig. 1.1**(c)**. Therefore, irrespective of the initial state, by shining the green laser on the NVC and exciting it into any of the states in the excited manifold, after decay it is most likely that it has been prepared in $|m_s = 0\rangle_g = |0\rangle$, providing a starting point from which to perform computation.

The difference in energy between our defined computational basis states $|0\rangle$ and $|1\rangle$ is ~ 2.87GHz, i.e. it is addressible by microwave (MW) radiation. Via antenna, we can deliver a MW pulse upon the NVC, driving the NVC between the two levels providing an implementation of an X-gate. Likewise, having initialised the state to $|0\rangle$, we can perform a $\pi/2$ rotation about the logical z-axis, by running the MW laser for half the time, resulting in the state $|+\rangle$. We can similarly devise MW radiation to achieve quantum gates and operations on our NVC qubit. We depict these cycles in Fig. 1.1c.

We can further exploit the decay mechanism to compose a readout procedure, to infer the population of $\{|0\rangle, |1\rangle\}$ at a given instant, for example following the application of a series of gates (a circuit) to the system. We know that the excitation due to the green laser is spin-preserving, i.e. when the NVC has been excited to $|m_s = 0\rangle_e$, it had originated in $|m_s = 0\rangle_g$. We also know that the decay $|m_s = 0\rangle_e \to |m_s = 0\rangle_g$ is spin preserving, with the emission of a red photon: by simply counting the number of excess[1] photons emitted, we quantify the population of $|0\rangle$ at the time of query. On the contrary, when the $|m_s = -1\rangle_g$ is excited, spin is also preserved, so it goes to $|m_s = -1\rangle_e$, but $|m_s = -1\rangle_e$ decays through the shelving state as outlined earlier, *without* the emission of a red photon (the decay emits out infrared radiation instead). We can hence infer the population of $|m_s = -1\rangle_g$ at the time of query by the fraction of incidents which don't emit a photon [10]. That is, say we first calibrate the system by retaining the green laser for some time: after a few μs, a steady state is achieved where the majority of the time, the triplet is in the computional state $|0\rangle = |m_s = 0\rangle_g$. Then, excitation from the same laser results in the excitation to $|m_s = 0\rangle_e$, which decays back to $|m_s = 0\rangle_g$ and emits a photon in the process; by counting the red photons emitted in a certain time window – equivalently, measuring the photoluminescence (PL) signal – we benchmark the population of $|0\rangle$ when nothing else has happened as p_0. Now, when we apply gates (i.e. MW pulses) to the NVC, we can similarly read out the population of $|0\rangle$ as p_0', and infer that the likelihood that the NVC is found in the

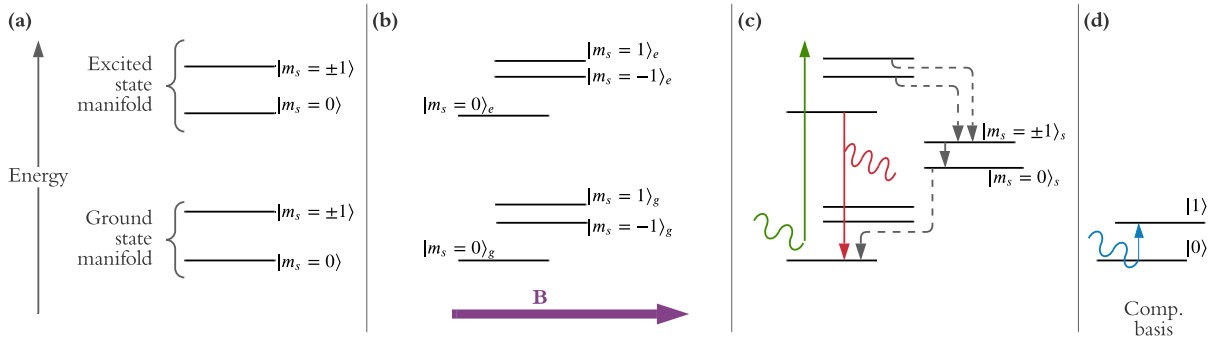

Figure 1.1: Simplified depiction of energy levels of the nitrogen-vacancy centre, corresponding to its triplet state. **a**, With no external magnetic field, the system has excited and ground-state manifolds, each of which consist of two energy levels depending on the magnetic spin, m_s. **b**, In the presence of a magnetic field (purple, B), the magnetic spins have distinct energy levels, i.e. Zeeman splitting giving distinct m_s. States are denoted by their magnetic spin, m_s and subscripted by their manifold (e for excited and g for ground-state). **c**, Application of a 532 nm laser (green arrow) excites the nitrogen-vacancy centre from any of the states in the ground state manifold into the excited manifold. The dominant decay mechanism for the excited states are shown: (i) $|m_s = 0\rangle_e \rightarrow |m_s = 0\rangle_g$ (photoluminescence, red) through the emission of a photon at 637 nm); (ii) $|m_s = \pm 1\rangle_e \rightarrow |m_s = 0\rangle_g$ (dotted grey lines) via the shelving manifold which allows for non-spin-preserving transition, emitting a photon in the infrared (not shown). **d**, Computational basis states $|0\rangle$ and $|1\rangle$ are assigned to the two lowest energy states. The difference in energy between these states is such that a microwave (MW, blue) can drive transition from $|0\rangle \leftrightarrow |1\rangle$. MW pulses can also be used to achieve other states apart from the basis states, allowing for the implementation of quantum logic gates.

initial state $|0\rangle$ is p_0'/p_0. We can use this quantity as the likelihood within quantum likelihood estimation (QLE), allowing us to learn from the NVC, as we will discuss in the next sections.

In summary then, by assigning basis states $|0\rangle, |1\rangle$ to energy levels of the ground state manifold, we are able to ensure the preparation of the NVC in $|0\rangle$ by first shining a green laser on the NVC. We can then apply MW radiation to achieve quantum logical gates on the system, and read out the final state of the system, again by shining a green laser and observing the PL (i.e. the emitted photons), and inferring the population level of each basis state. We represent these concepts in a simplified format in Fig. 1.1.

1 A large number of photons are emitted by the NVC when it is excited by a 532 nm laser, which can be profiled by its emission spectrum. At the *zero phonon line* (637 nm), a relatively large number of photons are emitted, compared with nearby wavelengths. This is where decay from the excited to ground state occurs without interacting with proximal phonons, as is the case during the spin-preserving decay $|m_s = 0\rangle_e \rightarrow |m_s = 0\rangle_g$. The excess photons are taken as indication that the electron had been in the state $|m_s = 0\rangle_e$ immediately prior to emission.

1.1.1 *Experimental procedure*

As our primary objective, we aim to model the decoherence and precession of the NVC (described in Section 1.2), and therefore must implement an experimental strategy which highlights the decoherence effects dominating the spin. The *Hahn echo sequence* is a series of operations which decouple a spin from the slowly varying components of its environment, i.e. the nuclear bath [11–15]. For short evolution times, i.e. in the first decay of the NVC, the spin is influenced mostly by *fast* decoherence processes, providing a platform to study the contributions of dominant decoherence effects in isolation.

During the Hahn echo sequence, the NVC spin undergoes a series of evolutions – either according to application of quantum logic gates or the natural evolution of the system interacting with its environment. Intuitively, the stages are as follows:

(a) Prepare spin in $|0\rangle$.

(b) Apply a $\pi/2$ MW pulse. A π-pulse is a MW pulse of sufficient duration to flip the spin completely ($|0\rangle \leftrightarrow |1\rangle$), so a $\pi/2$-pulse generates a superposition, i.e. $\pi/2 : |0\rangle \rightarrow |+\rangle$.

(c) The superposition precesses freely for t. During this time, the $|1\rangle$-component of the superposition picks up a phase proportional to t, such that the spin is now in the state $\frac{1}{\sqrt{2}}\left(|0\rangle + e^{-i\delta t}|1\rangle\right)$.

(d) A MW π-pulse is applied, which inverts the basis states, yielding the state $\frac{1}{\sqrt{2}}\left(|1\rangle + e^{-i\delta t}|0\rangle\right)$.

(e) The spin is again allowed precess freely, here for a duration t'. Again the $|1\rangle$-copmonent gains a phase $e^{-i\delta t'}$, i.e. the spin is in the state $\frac{1}{\sqrt{2}}\left(e^{-i\delta t}|0\rangle + e^{-i\delta t'}|1\rangle\right)$.

(f) A final $\pi/2$ pulse is applied, giving $\frac{1}{\sqrt{2}}\left(e^{-i\delta t}|+\rangle + e^{-i\delta t'}|-\rangle\right)$. Expanding $|+\rangle, |-\rangle$ and factoring $e^{-i\delta t}$, we get the final state

$$|\psi_H(t,t')\rangle = \frac{e^{-i\delta t}}{2}\left\{\left(1 + e^{-i\delta(t'-t)}\right)|0\rangle + \left(1 - e^{-i\delta(t'-t)}\right)|1\rangle\right\}. \tag{1.1}$$

If the second free evolution is run for $t' = t$, we retrieve

$$|\psi_H(t,t'=t)\rangle = \frac{e^{-i\delta t}}{2}\left\{(1+1)|0\rangle + (1-1)|1\rangle\right\} = |0\rangle, \tag{1.2}$$

i.e. the phase accumulated is effectively removed. This is therefore an excellent scheme when seeking to isolate the spin from its environment, e.g. when the spin is intended to act as a qubit. In practice it is impossible to decouple the environment entirely, since distant nuclei still interact with the spin, causing decoherence on a relatively long time scale[2]. These are what we refer to as

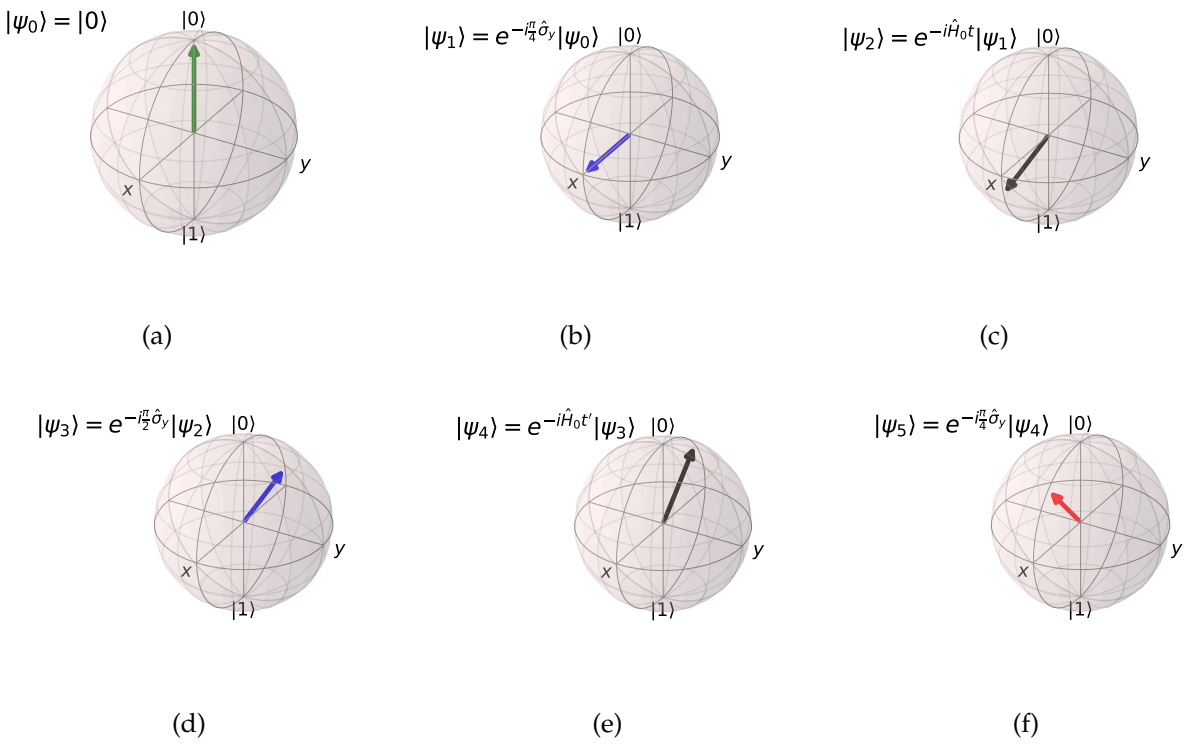

Figure 1.2: States of spin qubit at each stage of Hahn echo sequence shown on the Bloch sphere. **a,** The state of the NVC spin is initialised by a green laser into state $|\psi_0\rangle = |0\rangle$. **b,** We apply a $\pi/2$ rotation about the y-axis (i.e. a MW (microwave) pulse, implemented as $e^{-i\frac{\pi}{4}\hat{\sigma}_y}$), yielding the state $|\psi_1\rangle = |+\rangle$. **c,** The system is allowed to evolve according to its own $\hat{H}_0$ for t, $|\psi_2\rangle = e^{-i\hat{H}_0 t}|+\rangle$. **d,** We apply a second MW pulse, this time for a π-rotation about the y-axis, $|\psi_3\rangle = e^{-i\frac{\pi}{2}\hat{\sigma}_y}e^{-i\hat{H}_0 t}|+\rangle$. **e,** Again the system evolves according to interactions with the environment, this time for t'. **f,** We apply a final $\pi/2$ MW pulse to rotate about the y-axis again, projecting it upon $|0\rangle$. Here $|\psi_5\rangle$ is roughly half way between $|0\rangle$ and $|+\rangle$, i.e. along the z-axis. The spin is read out from $|\psi_5\rangle$ via the NVC's photoluminescence. Here $\hat{H}_0 = 0.25\,\hat{\sigma}_y$ was evolved for $t = 0.5$ (arbitrary units), and the final state overlap with the initial state, i.e. the likelihood of measuring the spin in $|0\rangle$ is $\Pr(0|\hat{H}_0, t) = 0.865$.

slow interactions: this decoupling scheme can therefore be viewed as corresponding to a model where the Hamiltonian consists solely of slow terms, enabling us to study the spin's interactions with its environment beyond the nearest C atom. We will explore this possibility in Chapter 2.

On the other hand, when $t' \neq t$, the spin is instead found in the state

$$|\psi_H(t, t' \neq t)\rangle = \frac{e^{-i\delta t}}{2}\left\{(1 + e^{-i\delta(t'-t)})\,|0\rangle + (1 - e^{-i\delta(t'-t)})\,|1\rangle\right\}. \tag{1.3}$$

Eq. (1.3) has the precise form (up to the phase factor $e^{-i\delta t}$) of a spin having undergone a *Ramsey sequence*, i.e. a $\pi/2$ pulse, followed by free evolution for t, and a final $\pi/2$ pulse. That is, for $t' \neq t$, the Hahn echo sequence behaves like a Ramsey sequence with a delay $(t' - t)$ [16]. $|\psi_H(t, t' \neq t)\rangle$ therefore does *not* decouple the spin from its dominant dephasing contributions, but rather it reverses the dephasing due to *slowly varying* components of the environment. As such, this provides a platform for examining only the *fast* effects on the spin, i.e. the dominant Markovian decoherence processes, which are expected to be dominated by coupling with the nearest C atom of strength $\mathcal{O}(\text{MHz})$.

In Chapter 2, we consider the system more broadly, and endeavour to characterise its coupling with several nuclei, located farther from the spin than the nearest C, i.e. the slower-varying contributions to the spin's dynamics, which an be examined via the former scheme with $t' = t$. For the remainder of this chapter, however, we will exploit the latter scheme, Eq. (1.3), in order to model the decoherence of the spin via its relationship with a single C atom.

To relate the experimental procedure to the parameter learning technique described in **??** which fulfils the training stage of QMLA, consider the overal Hahn echo sequence. We depict the stages of the experiment more generally in Fig. 1.2, starting from the initialised computational state, $|\psi_0\rangle = |0\rangle$, through to its final state which is read out through PL, both of which as described in Section 1.1. In particular, the final state, $|\psi\rangle_5$, is effectively read out by projection onto $|0\rangle$; we can interpret the normalised PL after evolution time t as the likelihood that the NVC is found in $|0\rangle$ after evolution of its *true*[3] Hamiltonian, $\hat{H}_0$ for t. That is, we assign this projection as the quantity $\Pr(0|\hat{H}_0, t)$ (the likelihood), and it can be used within likelihood estimation in order to refine a candidate model $\hat{H}_j$, effectively[4] by changing the structure of $\hat{H}_j$ until $\Pr(0|\hat{H}_0, t) \approx \Pr(0|\hat{H}_j, t)\ \forall t$.

By varying the evolution time, t, used within the Hahn echo sequence, we can map the likelihood against time, which we can view as capturing the *dynamics* of the NVC spin, Fig. 1.3. We vary the evolution time up to $t \sim 4\mu s$ in intervals of $\Delta t = 50$ns, so we have 425 data points. Note the data for the studied NVC is taken once and analysed offline, i.e. QMLA does not have

2 The timescales on which these interactions decohere the spin are orders of magnitude higher then available through alternative decoupling schemes, e.g. $T_2 = 242\,\mu$s in [12].

3 Note: we refer to the target $\hat{H}_0$ as the system's *true* Hamiltonian. This is a matter of convention: here $\hat{H}_0$ is not the Hamiltonian of the complete NVC system/environment, but captures only the precession and fast decoherence processes, i.e. $\hat{H}_0$ is simply the name assigned to the Hamiltonian which models the interactions we aim to uncover.

4 Of course this is a gross simplification of quantum Hamiltonian learning (QHL) which is described fully in **??**

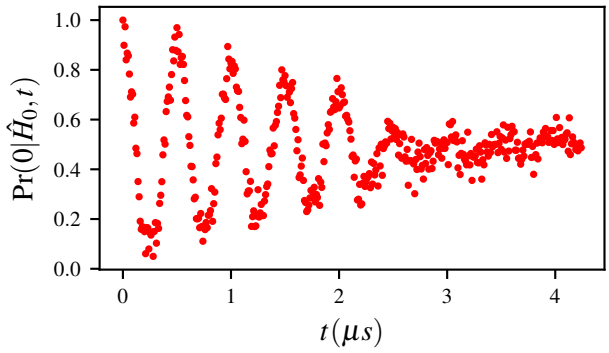

Figure 1.3: Raw data for the nitrogen-vacancy centre's dynamics. The y-axis shows the normalised photoluminescence of the NVC, equivalently the likelihood $\Pr(0|\hat{H}_0, t)$.

complete authority to design experiments to run on the NVC, although it can aim to choose the most informative t available in the predefined set; we will discuss the consequences of this restriction in Section 1.4.

1.2 TARGET SYSTEM

We take the axis of the NVC, i.e. the axis connecting the ^{14}N with the lattice vacancy, as the z-axis. While the NVC is subject to myriad interactions which result in decoherence, we choose to focus on its dominant interactions with proximal environmental nuclei. These interactions are characterised by hyperfine terms [17]. The complete Hamiltonian for such systems, where the set of nuclear sites is $\{\chi\}$, is expected to be given by

$$\hat{H}_{\text{full}} = \Delta_{\text{gs}}\hat{S}_z^2 + \mu_B g\mathbf{B}\cdot\mathbf{S} + \mathbf{S}\cdot\sum_{\chi}\left(\mathbf{A}_\chi\cdot\hat{I}_\chi\right) + P\hat{I}_z^2 + \mu_n g\mathbf{B}\cdot\sum_{\chi}\hat{I}_\chi. \tag{1.4}$$

Our overarching intention is to design an approximate model $\hat{H}'$, i.e. a subset of the terms in $\hat{H}_{\text{full}}$ which can explain the observed dynamics and decoherence of the NVC. It is therefore prudent only to retain terms which *may* contribute to the spin's decoherence and precession. First, we will describe each term in Eq. (1.4), as well as approximations which enable us to drastically reduce the space of terms to consider for inclusion in $\hat{H}'$.

ISOLATED-SPIN TERMS

Describe the spin independent of the environmental nuclei

- $\Delta_{\text{gs}}\hat{S}_z^2$: the *zero-field* splitting, or ground state splitting between the computational basis states. $\Delta_{\text{gs}} \sim$ GHz is a constant offset which does not contribute to the decoherence, so it is excluded from our study.
- $\mu_B g\mathbf{B}\cdot\mathbf{S}$: the spin's precession about the magnetic field, $\mathbf{B} = \left(B_x\ B_y\ B_z\right)$, via the total spin operator[5] $\mathbf{S} = \left(\hat{S}_x\ \hat{S}_y\ \hat{S}_z\right)$, where μ_B is the Bohr magneton and g is the electron g-factor (≈ 2, simplified from the g-factor tensor). Misalignment of the magnetic field is a decoherence effect, so one core aim of QMLA in this setting is to identify whether such terms dominate.

HYPERFINE TERMS

- $\hat{S}\cdot\sum_\chi\left(\mathbf{A}_\chi\cdot\hat{I}_\chi\right)$: The NVC total spin operator $\mathbf{S}$ couples the spin with each site, χ. At each site there is a nucleus which has total spin operator $\mathbf{I}_\chi = \left(\hat{I}_x\ \hat{I}_y\ \hat{I}_z\right)_\chi$. $\mathbf{A}$ is the hyperfine tensor, containing the hyperfine parameters of interest. The coupling between the NVC and these nuceli is one of the primary decoherence mechanisms, so is essential to any model aiming to capture those dynamics.

BATH-ONLY TERMS

Describe the other nuceli independent of the spin

- $P\hat{I}_z^2$: the quadrupole splitting, which provides another constant shift, and is therefore not of interest when modelling the spin's decoherence, and can be neglected.

– $\mu_n g \mathbf{B} \cdot \sum_\chi \hat{I}_\chi$: nuclear precession terms. μ_n is the nuclear magneton and g is the nuclear g-factor (again from the g-factor tensor). These terms represent the nuclei independent of the spin – these terms lead to decoherence at much higher times than we have access to, since the Hahn echo sequence decouples the spin from the bath. For the short-time model targeted here, then, these terms can be excluded.

Given that we are modelling the spin's decoherence, we are interested only in the spin and its interactions with the environment, so we can immediately drop the bath-only terms, by assuming the bath is static apart from its interactions with the NVC. This is a usual assumption in the treatment of open system dynamics, to allow for focus on the dominant interactions in the processes of interest [18]. Additionally, since the zero field splitting contributes a constant shift in energy, we can safely omit it by moving to the rotating frame. We are then left only with the second and third terms of Eq. (1.4), from which to define the space of terms in which QMLA will search:

$$\mu_B g \mathbf{B} \cdot \mathbf{S}; \tag{1.5a}$$

$$\mathbf{S} \cdot \sum_\chi \left(\mathbf{A}_\chi \cdot \hat{\mathbf{I}}_\chi \right). \tag{1.5b}$$

1.2.1 *Mapping to model terms*

Next we will focus on mapping the remaining terms to operators to compose the set of terms $\mathcal{T}$ to use in our ES. In our modelling, the NVC spin is represented by the first logical qubit, with a further $|\{\chi\}|$ qubits, each representing a unique nuclear site, as discussed later in this section. As standard, we take the axis[6] of the NVC as parallel to the qubit's z-axis.

The first terms included, Eq. (1.5a), come from the spin's precession about the magnetic field. It is usually assumed that the external, applied magnetic field is well-aligned with the spin qubit's z-axis: if the field is misaligned, it leads to decoherence effects. Determining the alignment is treated as a core role of QMLA, i.e. we will endeavour to establish whether the x-, y-axis components of the magnetic field are important for describing the spin's decoherence. Then, we have

$$\mu_B g \mathbf{B} \cdot \mathbf{S} = \mu_B g (B_x \quad B_y \quad B_z) \cdot (\hat{S}_x \quad \hat{S}_y \quad \hat{S}_z) \rightarrow \alpha_x \hat{S}_x + \alpha_y \hat{S}_y + \alpha_z \hat{S}_z, \tag{1.6}$$

with $\alpha_i = \mu_B g B_i$. The spin's rotation terms to be included in QMLA's deliberations are therefore

$$\mathcal{T}_s = \{\hat{S}_x, \ \hat{S}_y, \ \hat{S}_z\}. \tag{1.7}$$

5 We invoke an inexact representation of high dimensional tensors here for ease of interpretation. For instance, the total nuclear spin operator exists in arbitrary dimension (depending on the number of sites modelled), but we present it simply as $\mathbf{I} = (\hat{I}_x \ \hat{I}_y \ \hat{I}_z)$ at each site to convey that we can separate the terms in the construction of models.

6 The quantisation axis, i.e. the axis along the ^{14}N and lattice vacancy.

Next, we consider the hyperfine coupling term. In general we sum over the nuclear sites $\{\chi\}$, since the NVC spin will interact with every nucleus within a certain range. We show in [1] that a realistic system requires modelling a finite-size bath of $|\{\chi\}| \sim 15$ nuclei to capture the dynamics of interest, which is infeasible for complete characterisation via classical simulation, where we are limited to ~ 11 qubit calculations[7]. Instead, by focusing only on the *short-time* dynamics of the NVC, we can isolate the effects of dominant interactions, most notably with a single nearby C. Indeed, by assigning a first qubit as representing the NVC spin, we can map the entire environment onto a generic second *environmental qubit*, representing the amalgamation of said interactions, though we can think of the two-qubit system as the NVC coupled with a single ^{14}N [17].

$$\mathbf{S} \cdot \sum_{\chi} (\mathbf{A}_{\chi} \cdot \mathbf{I}_{\chi}) \rightarrow \mathbf{S} \cdot \mathbf{A} \cdot \mathbf{I} \tag{1.8}$$

This reduces the dimension of our approximation: the number of qubits required, n_q reduces from $n_q = 1 + |\{\chi\}|$ to $n_q = 2$, since now we only retain qubits for the NVC and the ^{14}N (which also represents the entire bath). The hyperfine tensor $\mathbf{A}$ consists of the hyperfine parameters, i.e. the strength of correspdoning interactions.

$$\mathbf{A} = \begin{pmatrix} A_{\perp} & 0 & 0 \\ 0 & A_{\perp} & 0 \\ 0 & 0 & A_{\parallel} \end{pmatrix}, \tag{1.9}$$

where $A_{\perp}$ is the non-axial hyperfine coupling term and $A_{\parallel}$ is the axial coupling term, since the axis of the NVC is used to define the z-axis for our qubits.

The total spin operators are then those of the NVC operating on the first logical qubit, e.g. $\hat{S}_x^{(1)}$, and those of the environmental qubit on the second, e.g. $\hat{I}_x^{(2)}$. They can be summarised as

$$\begin{aligned} \mathbf{S} &= (\hat{S}_x^{(1)} \quad \hat{S}_y^{(1)} \quad \hat{S}_z^{(1)}) \\ \mathbf{I} &= (\hat{I}_x^{(2)} \quad \hat{I}_y^{(2)} \quad \hat{I}_z^{(2)}) \end{aligned} \tag{1.10}$$

So we can write,

$$\begin{aligned} \mathbf{S} \cdot \mathbf{A} \cdot \mathbf{I} = & A_{\perp} \hat{S}_x \hat{I}_x + A_{\perp} \hat{S}_y \hat{I}_y + A_{\parallel} \hat{S}_y \hat{I}_y \\ & + A_{xy} \left(\hat{S}_x \hat{I}_y + \hat{S}_y \hat{I}_x \right) \\ & + A_{xz} \left(\hat{S}_x \hat{I}_z + \hat{S}_z \hat{I}_x \right) \\ & + A_{yz} \left(\hat{S}_y \hat{I}_z + \hat{S}_z \hat{I}_y \right) \end{aligned} \tag{1.11}$$

Similarly to α_i in Eq. (1.6), we replace the expected (and theoretically computable) scalar parameters, e.g. $A_{\perp}$, with generic parameters α, to be learned. Off-diagonal terms, referred to hereafter as *transverse* terms ($\hat{S}_i \hat{I}_j$ where $i \neq j$), are usually neglected [11]. Here we will employ QMLA to determine whether the transverse contributions are worthy of inclusion in

the decoherence model, although we consider only $\{\hat{S}_x\hat{I}_y, \hat{S}_x\hat{I}_z, \hat{S}_y\hat{I}_z\}$ for brevity. The hyperfine terms to be entertained by QMLA are then

$$\mathcal{T}_{HF} = \begin{Bmatrix} \hat{S}_x\hat{I}_x, & \hat{S}_y\hat{I}_y, & \hat{S}_z\hat{I}_z, \\ \hat{S}_x\hat{I}_y, & \hat{S}_x\hat{I}_z, & \hat{S}_y\hat{I}_z \end{Bmatrix}. \tag{1.12}$$

Finally, combining Eq. (1.7) and Eq. (1.12), we have the full set of terms to incorporate into the ES for the QMLA model search:

$$\mathcal{T}_{\text{NV}} = \begin{Bmatrix} \hat{S}_x, & \hat{S}_y, & \hat{S}_z, \\ \hat{S}_x\hat{I}_x, & \hat{S}_y\hat{I}_y, & \hat{S}_z\hat{I}_z, \\ \hat{S}_x\hat{I}_y, & \hat{S}_x\hat{I}_z, & \hat{S}_y\hat{I}_z \end{Bmatrix}. \tag{1.13}$$

We introduce a shorthand notation to ease model representation for the remainder of this chapter. Recall that we have defined a two-qubit Hilbert space for model construction. Terms which affect only the spin act only on the first qubit, $\hat{S}_i = \hat{S}_i^{(1)} = \hat{\sigma}_i \otimes \hat{\mathbb{1}}$, where $\hat{\sigma}_i$ is the Pauli operator giving rotation about the i-axis, and $\hat{\mathbb{1}}$ is the one-qubit identity matrix. Retaining the hyperfine notation, for the expectedly-dominant diagonal terms, we denote $\hat{A}_i = \hat{S}_i^{(1)}\hat{I}_i^{(2)} = \hat{\sigma}_i \otimes \hat{\sigma}_i$. We refer to the transverse terms as $\hat{T}_{kl} = \hat{S}_k^{(1)}\hat{I}_l^2 = \hat{\sigma}_k \otimes \hat{\sigma}_l$. We can hence rewrite Eq. (1.13) as

$$\mathcal{T}_{\text{NV}} = \begin{Bmatrix} \hat{S}_x, & \hat{S}_y, & \hat{S}_z, \\ \hat{A}_x, & \hat{A}_y, & \hat{A}_z, \\ \hat{T}_{xy}, & \hat{T}_{xz}, & \hat{T}_{yz} \end{Bmatrix}. \tag{1.14}$$

We also use a succinct representation for brevity, e.g. $\hat{S}_{xy}\hat{A}_z = \hat{S}_x + \hat{S}_y + \hat{A}_z$, where parameters $\alpha_x, \alpha_y, \alpha_z$ are implicitly assumed.

1.2.2 *Prior knowledge*

QMLA will construct models using the pool of terms defined in Eq. (1.14). Recall from **??** that each model considered must be trained independently, where the purpose of model training is to optimise the parameter vector $\vec{\alpha}$ which characterises the model. For example, the model $\hat{H}_i = \hat{S}_{x,y}\hat{A}_z = \alpha_1\hat{S}_x + \alpha_2\hat{S}_y + \alpha_3\hat{A}_z$, is trained to retrieve the optimal $\vec{\alpha}' = (\alpha_1' \quad \alpha_2' \quad \alpha_3')$. Models are trained through QHL, described in **??**, which iteratively updates a probability distribution for the associated parameters, $\Pr(\vec{\alpha})$. As such, a *prior* distribution must be drawn, from which QHL begins its training. While QHL can redraw the probability distribution iteratively, and even find parameters entirely outside of the initial range, it is necessary at least to identify the order

7 This limitation arises from the requirement to compute the total evolution of the global state, involving calculation of $e^{-i\hat{H}t}$, i.e. the characterisation of an n_q-qubit model depends on classical exponentiation of the $2^{n_q} \times 2^{n_q}$ Hamiltonian for each particle and experiment in classical likelihood estimation (CLE), which is a prohibitively expense.

of magnitude where the true parameter should be found. The algorithm therefore demands that the user specifies the *range* of each parameter in which to search, which can be based on domain knowledge and theoretical predictions. For example, recall from Section 1.2 that the zero field splitting, Δ_{gs} in Eq. (1.4) (and excluded in our modelling), is expected to be $\sim$ GHz: in order to provide a reasonable chance at learning the true parameter, here we would propose a prior distribution of 5 ± 2GHz. We must similarly identify the rough range in which we reasonably expect to find parameters associated with each term in Eq. (1.14).

The spin-only terms, $\hat{S}_i$, are consequences of the magnetic field, expected in the range $\sim 2 - 3$MHz. Likewise, the hyperfine terms, $\hat{A}_i$ are expected in the range of $\sim$ MHz [19], while in the *secular approximation* only the z-component is expected to contribute substantially [20]. The non axial hyperfine terms, i.e. the transverse terms $\hat{T}_{kl}$ are not usually included in effective models, but can be found of order $\mathcal{O}(10\text{kHz})$ [21]. We utilise this prior understanding of the system to inform the parameter range used for training candidate models: for each of the terms in Eq. (1.14), we will adopt a normal prior distribution of 4 ± 1.5MHz. This range is sufficiently specific to ensure the training subroutine operates in a physically meaningful – and likely appropriate – space, while also broad enough to allow for significant differences between expectation and reality. Moreover this distribution supports hypotheses where each parameter is zero: if these prove favourable, negligible contributions can be identified and excluded from the model.

1.3 EXPLORATION STRATEGY

We may now turn to the specific implementation details by which QMLA is applied to the study of this NVC system. Recalling the terminology of QMLA from **??**, we design an exploration strategy (ES) specifically for the system under study. The ES will account for the details listed in this chapter so far, in summary:

- we aim to assign a model, $\hat{H}'$, to the NVC to describe its decoherence processes
  - we especially focus on its hyperfine interactions;
- we use a 2-qubit approximation
  - the first qubit represent the spin itself;
  - the second qubit represents the environment in which the NVC resides;
- we query the NVC by performing Hahn echo experiments (Fig. 1.2);
- the outcome of those experiments are thought of as the system's likelihoods (Fig. 1.3);
- candidate models are composed of the terms defined in Eq. (1.14)
  - likelihoods are used for the training of individual candidate models through QHL;
  - we assign approximate ranges to the scalar parameters corresponding to each term based on theoretical arguments;

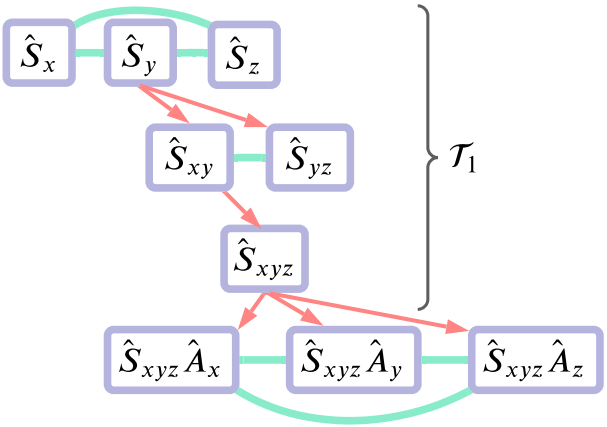

Figure 1.4: Greedy model search. Models (purple) are placed on branches, trained and consolidated (green) as in **??**, with the branch champion spawning (red) candidates to place on the subsequent branch. Branches are grouped in tiers, correspdoning to levels of approximation: the first tier of the model generation strategy is shown, where $\mathcal{T}_1 = \{\hat{S}_x, \hat{S}_y, \hat{S}_z\}$ is explored. The final champion from the first tier seeds the second tier.

* those parameters are to be learned precisely by QHL.

As outlined in **??**, the central role of any ES is to specify the model generation procedure, which QMLA relies upon for deciding the next set of candidate models to test. In this case, we exploit some intuition and prior knowledge of how such systems work, to design a bespoke model generation subroutine: we can think of this as a midway point between the completely specified ESs used for identifying the underlying lattices from a prescribed set in **??**, and the entirely general genetic algorithm which does not restrict model generation, of **??**. We use the standard structure of exploration trees (ETs) introduced in **??**, where models are placed on consecutive branches, μ, and branches are consolidated by pairwise comparisons between all models on μ, where comparisons are computed through Bayes factors (BFs). The outcome of consolidation on μ is the determination of a single *branch champion*, $\hat{H}_{C(\mu)}$.

We use a *greedy search rule*: terms are added one-by-one to gradually increase the complexity of candidate models until terms are exhausted [22]. We break the ET into three distinct tiers, each corresponding to an intuitive degree of complexity: the first tier involves the spin-only terms, $\mathcal{T}_1 = \{\hat{S}_i\}$; the second considers the hyperfine terms, $\mathcal{T}_2 = \{\hat{A}_i\}$; the final tier the transverse terms, $\mathcal{T}_3 = \{\hat{T}_i\}$. Within each tier, terms are added greedily to the previous branch's champion, $\hat{H}_{C(\mu)}$. So, the first branch is given by $\mu = \{\hat{S}_x, \hat{S}_y, \hat{S}_z\}$; say $\hat{H}_{C(\mu)} = \hat{S}_y$, then $\mu + 1$ determines that $\hat{S}_x, \hat{S}_z$ are not yet considerd, so it constructs the models $\{\hat{S}_{x,y}, \hat{S}_{y,z}\}$, e.g. Fig. 1.4. After exhausting all tiers, we consolidate the set of branch champions, $\mathbb{H}_C = \{\hat{H}_{C(\mu)}\}$, to determine the best model considered globally, $\hat{H}'$.

Clearly, this growth rule is partially deterministic, insofar as some models are gauranteed to be considered, while others are not reachable. Indeed, the space of available models are heavily constrained, in particular models in later tiers will always involve all of the tier 1 terms, e.g. $\hat{S}_x \hat{A}_y$ can not occur organically. In general, restrictions of this kind undermine the ES and are considered a weakness. To account for this, we add a final test of reducibility on the champion model, triggered if any of the parameters of $\vec{\alpha}'$ are potentially negligible, i.e. the posterior distribution of any parameter assigns credibility to the hypothesis that the parameter is 0. This champion reducibility test simply removes the negligible-parmeter terms from $\hat{H}'$, yielding a reduced global champion, $\hat{H}'_r$. We then compute the BF between $\hat{H}', \hat{H}'_r$: if the BF indicates strong evidence in favour of the reduced version, we replace the champion model, $\hat{H}' \leftarrow \hat{H}'_r$. In effect, we thus verify the statistical significance of each term included in $\hat{H}'$.

The total model in Eq. (1.4) supports $N_t = 1 + 3 + 6|\chi| + 3 + 3|\chi| = 7 + 9|\chi|$ terms, which we reduced to a space of $N_t = 3 + 6|\chi| = 9$ through several approximations[8]. Even so, the remainng 2^9 permitted models were reduced further by building the logic of this ES from our intuition aroud existing knowledge of typical NVC systems. As such, the described ES will only ever consider < 20 models per instance. The described ES seems overly perscriptive, but should be viewed as a first attempt at a generalisable approach: essentially we can view the tiers of the greedy search as characterising the system at various approximations, e.g. the first tier examines one-qubit terms, while subsequent tiers inspect 2-qubit terms. We can envision future work where the greedy search is gradually extended to less rigid approximations, enabling study of more complex quantum systems. This leads to some important remarks:

1. Realistic, near-term applications of QMLA can not be thought of as a solution to black-box characterisation problems: it must be used in conjunction with domain expertise for the system under study.
2. While this test-case yields promising results, the outcome of QMLA here may not be especially insightful, since the available model terms were so deliberately constrained – we demonstrate a use-case in Chapter 2 where a broader scope is enabled in simulation.

A common charge against QMLA supposes to first write down the most complex model, train it fully, and then infer which terms are negligible, in a similar process to the champion reduction test outlined here. While this may be feasible in the case described here, with $N_t = 9$ and a closed term set, it is unscalable: adding just a second nuclear site increases the model search to a space of $N_t = 15$. Models of higher cardinality ($|\vec{\alpha}|$) demand higher N_E, N_P to train well, so immediately training the most involved model would require infeasible resources[9], and risks significantly overfitting the data. It seems more appropriate to work "from the ground up", testing terms and only keeping those justified, rather than training all terms and attempting to decouple their effects post-hoc.

9 Note: in the case studies presented in this thesis, it was found that the same resources were sufficient for the simplest and most complex models, due to the relatively small number of terms therein. We expect for larger models, e.g. $|\vec{\alpha}| > 10$, that the resources allocated ought to be proportional to the cardinality, which is an in-built option in the QMLA software.

1.3.1 *Test in simulation*

Before considering the real experimental data (Fig. 1.3), we first test the ES in simulation under ideal conditions. That is, we assume the ability to prepare arbitrary probe states, and use a random probe set (see **??**), and use the full expectation value as the likelihood, $|\langle\psi|e^{-i\hat{H}_j t}|\psi\rangle|^2$. Of course, this is infeasible since we presume access to the full state at the time of measurement, but this can be seen as a best-case scenario for this application, because the realistic case loses information by tracing out the environmental qubit at measurement. We vary the target $\hat{H}_0$, among a series of ten models, which are all valid models achievable by the ES.

1.4 EXPERIMENT DESIGN CONSTRAINTS

Moving to analyse the experimental setup, there are a number of constraints which we must account for in training models. Firstly, the $\pi/2$-pulse applied to the prepared qubit ($|\psi_0\rangle \rightarrow |\psi_1\rangle$ in Fig. 1.2) means that the state before evolution is always $|+\rangle$ in the computational basis; this is a severe limitation on model training, as we saw in **??**. Moreover, this places a bias on the interactions QMLA is likely to identify: we show in Fig. 1.2 how QHL performs in training the same model using (i) the probe set available experimentally; (ii) a more general (random) probe set. This bias adds a caveat to the outcome of this study: the suppression of terms means we are more likely to find some genuine interactions than others, so the champion model is capturing the decoherence with respect only to one basis.

The experiment was run with increasing t for the duration of the first decay of the NVC, i.e. until it had dephased, so the data available for examination terminate at $t_{\max} \sim 4\mu s$, see Fig. 1.3. As discussed in **??**, usually it is helpful to allow an experiment design heuristic (EDH) to choose the experimental controls, including the evoltuion time, t, against which the model is trained at each experiment; the default particle guess heuristic (PGH) attempts to select t at the upper boundary of times where the model is expected to be predictive, to maximise the information gained by the experiment (see **??**). Here, however, we can not allow the EDH to select arbitrary t, since we do not have data beyond $t_{\max}$.

We require a custom EDH to account for the constraints outlined, with the following considerations:

1. We may only assume access to the probe $|+\rangle$ on the spin qubit
   (a) we further assume the environmental spin is polarised by the same microwave pulse, such that the global probe available is $|\psi\rangle = |+\rangle\,|+'\rangle$, with $|+'\rangle = \frac{|0\rangle + e^{i\phi}|1\rangle}{\sqrt{2}}$ and ϕ is random [23].
2. We can not allow the choice of any t:
   (a) Any $t > t_{\max}$, arising from a thin parameter distribution, must be mapped to some $0 < t \leq t_{\max}$.

(b) All nominated t must be mapped to the nearest available t in the dataset so that the likelihoods are as close as possible to simulating the true system.

3. Much of the physics of interest occurs at relatively high times, i.e. because the rotation (MHz) terms dominate, the decay of the peaks can be seen as evidence of the bath, notably through hyperfine terms in the model.

   (a) We therefore wish to enforce that all models are trained on those data ($t \geq 2\mu s$), even if their parameter distribution is insufficiently narrow to yield those times naturally.

Accounting for these, we construct an EDH which mixes the robust, adaptive nature of PGH, useful for refining an initially broad $\Pr(\vec{\alpha})$, with a primitive, linear time-selection, useful to ensure the trained parameters at least attempt to account for the physics we are actually interested in. That is, with each model trained for N_E experiments, we train according to the standard PGH for the first $N_e/2$, but force the training to mediate over the available data for the latter $N_e/2$.

1.5 RESULTS

We apply the ES described in Section 1.3 to the raw data of Fig. 1.3: the results are summarised in Fig. 1.5. We first focus on the overall outcomes: the most blunt figure of merit of interest is simply whether QMLA overfits or underits the true parameterisation. In preliminary analysis we run 500 instances with varying $\hat{H}_0$, varying the cardinality of $\hat{H}_0$, so we can broadly gauge the tendency towards over- and under-fitting: we see that in $\sim 50\%$ of instances the correct cardinality is found, rising to $\sim 86\%$ by allowing ± 1 term, Fig. 1.5**(b)**. In general, the champion models from each instance are highly predictive: the median *coefficient of determination* between the systems' and corresponding champion models' data is $R^2 = 0.84$.

Then, considering the performance of the algorithm on whole, we perform runs of 100 instances on the exerpimental data as well as simulated data, where the simulation assumes[10] $\hat{H}_0 = \hat{S}_{xyz}\hat{A}_z$. The set of models selected most frequently are shown in Fig. 1.5**(c)**, and each model is trained with $N_e = 1000, N_p = 3000$, with the volumes of those models (in the experimental case) shown in Fig. 1.5**d**. In particular, the most prominent models, $\{\hat{S}_{x,y,z}\hat{A}_z, \hat{S}_{x,y,z}\hat{A}_{y,z}, \hat{S}_{x,y,z}\hat{A}_{x,z}, \hat{S}_{y,z}\hat{A}_z\}$ are found collectively in 74% (87%) of instances on the experimental (simulated) data; the win rate and R^2 of all models (which won at least one instance) are reported in Table 1.1. It is noteworthy that even in the simulated case, the same models mislead QMLA: this suggests that the resultant physics from these models is substantially similar to that of the true model[11]. These models are defensible with respect to the descriptions of Section 1.2, since in each case they detect the interaction between the spin qubit and the

10 Here we work backwards by setting the target model as that which QMLA deemed most appropriate for the available data. We posit that this choice is arbitrary and doesn't fundamentally change the discussion of this chapter, merely aiding in analysing the performance of the algorithm with respect to a concrete example.

11 Alternatively, that the same systematic error misdirects the search in both cases.

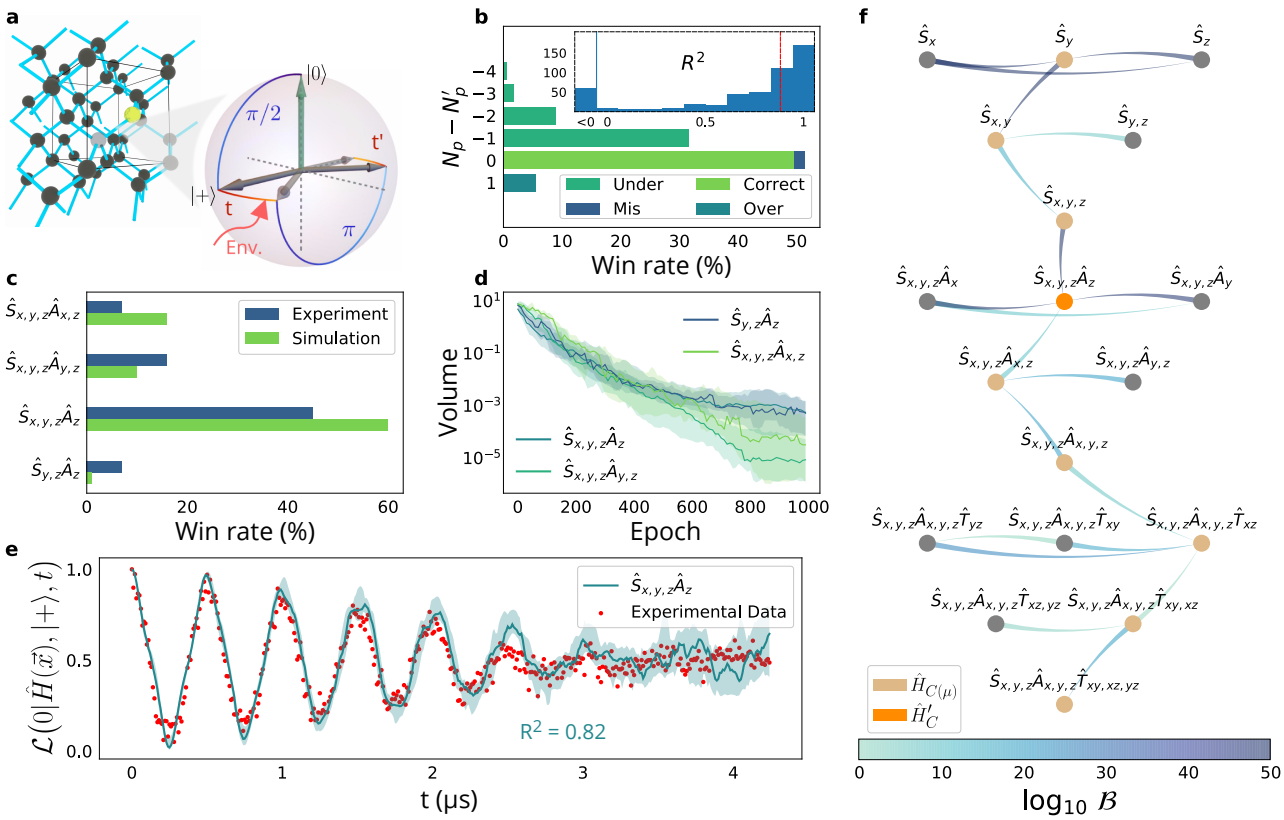

Figure 1.5: QMLA results on simulated and experimental data, describing a NVC (nitrogen-vacancy centre) system. Figure reproduced from [1]. **a**, The carbon lattice providing the outer environment for the NVC, along with the time evolution of the electron spin state (represented on a Bloch sphere) during the pulses for the Hahn echo sequences. These steps are expanded in Fig. 1.2, although here the final $\pi/2$ pulse is omitted. **b**, Simulation of 500 independent QMLA instances, where $\hat{H}_0$ is chosen randomly. The win rate is reported against the difference $(N_p - N'_p)$ between the number of parameters in $\hat{H}'$ and $\hat{H}_0$, respectively. The *under-parameterised (over-parameterised)* class refers to models with less (more) parameters than $\hat{H}_0$. *Correct* indicates that exactly $\hat{H}_0$ was found. The *mis-parameterised* class groups models with the same parametrisation cardinality as $\hat{H}_0$, but different Hamiltonian terms. **Inset**, Histogram of occurrences of R^2 values for each retrieved $\hat{H}'$ against a sampling of datapoints from $\hat{H}_0$. The blue vertical line groups together all those instance champions with $R^2 < 0$, and the median $R^2 = 0.84$ is shown as a red dotted line. **c**, Win rates of the top four models for 100 QMLA instances, against both simulated and experimental data. On experimental data, $\hat{H}_0$ is unknown, while simulations use $\hat{H}_0 = \hat{S}_{x,y,z}\hat{A}_z$. **d**, Total volume spanned by the parameters' probability distribution across progressive epochs, for the models in **(c)**. The shaded area show the 67% confidence region of volumes, taken from instances where those models were deemed $\hat{H}'$. **e**, Simulated likelihoods reproduced by the model with the highest win rate ($\hat{S}_{x,y,z}\hat{A}_z$, turquoise), compared with corresponding NV-centre system experimental data (red dots, extracted from the observed photoluminescence of the first Hahn echo decay). Error bars are smaller than the dots. The shaded area indicates the 67% confidence region of likelihoods predicted from the instances where $\hat{H}' = \hat{S}_{x,y,z}\hat{A}_z$ **f**, A single QMLA instance depicted as a directed acyclic graph. The thin end of each edge points to the favoured model; the colour of the edges depict the strength of evidence, $\log_{10}\mathcal{B}$, where $\mathcal{B}$ is the BF between those two models. Champions of each layer, $\hat{H}_{C(\mu)}$, are in light brown, whereas the global champion $\hat{H}'$ is in orange and all other candidate models are grey.

Model	Experiment		Simulation	
	Wins	R^2	Wins	R^2
$\hat{S}_{y,z}\hat{A}_z$	9	0.8	1	0.26
$\hat{S}_y\hat{A}_{x,z}$	2	0.63		
$\hat{S}_{x,y,z}\hat{A}_z$	45	0.86	61	0.97
$\hat{S}_{x,y,z}\hat{A}_y$			1	-0.54
$\hat{S}_{x,y,z}\hat{A}_{x,y}$	3	0.81		
$\hat{S}_{x,y,z}\hat{A}_{y,z}$	14	0.83	10	0.96
$\hat{S}_{x,y,z}\hat{A}_{x,z}$	6	0.64	15	0.99
$\hat{S}_{x,y,z}\hat{A}_{x,y,z}$	2	0.72	5	0.97
$\hat{S}_{x,y,z}\hat{A}_{x,z}\hat{T}_{xz}$			1	0.68
$\hat{S}_{x,y,z}\hat{A}_{x,y,z}\hat{T}_{xz}$			5	0.77
$\hat{S}_y\hat{A}_{x,y,z}\hat{T}_{xy,xz,yz}$	2	0.31		
$\hat{S}_{x,y,z}\hat{A}_{x,y,z}\hat{T}_{xy,xz}$	4	0.67	1	0.32

Table 1.1: QMLA win rates and R^2 for models based on experimental data and simulations. We state the number of QMLA instances won by each model and the average R^2 for those instances as an indication of the predictive power of winning models.

environmental qubit, i.e. the hyperfine terms $\hat{A}_i$, especially $\hat{A}_z$ which occurs in 97% (99%) of champion models, reported in Table 1.1. We discuss some physical insights from these results in Section 1.5.1.

The most frequently identified model, $\hat{H}' = \hat{S}_{x,y,z}\hat{A}_z$, is found in 45% (61%) of instances on experimental (simualted) data: we show its attempt to reproduce the dynamics of Fig. 1.3 in Fig. 1.5**(e)**, showing excellent agreement with the raw data, with $R^2 = 0.82$. This serves as an essential sanity check: we can intuitively see that QMLA has distilled a model which captures at least *some* of the most important physical interactions the target NVC system is subject to; otherwise we would not see such clear overlap between the predicted and true dynamics.

Finally we display the model search as a directed acyclic graph (DAG) in Fig. 1.5**(f)**, where models are represented on nodes on the graph's layers (equivalent to ET branches), and their parents are resident on the branch immediately above their own. Comparisons between models, $(\hat{H}_i, \hat{H}_j)$, are shown as edges between nodes on the graph, coloured by the strength of evidence of the outcome, i.e. the Bayes factor, B_{ij}. Each layer, μ, nominates their branch champion, $\hat{H}_{C(\mu)}$; the set of branch champions are consolidated to determine the global champion, $\hat{H}'_C$.

1.5.1 *Analysis*

Here we offer some further perspectives, considering the runs summarised in Fig. 1.5. Fig. 1.6 first details all models considered in the 200 instances comprising the experimental and simulated

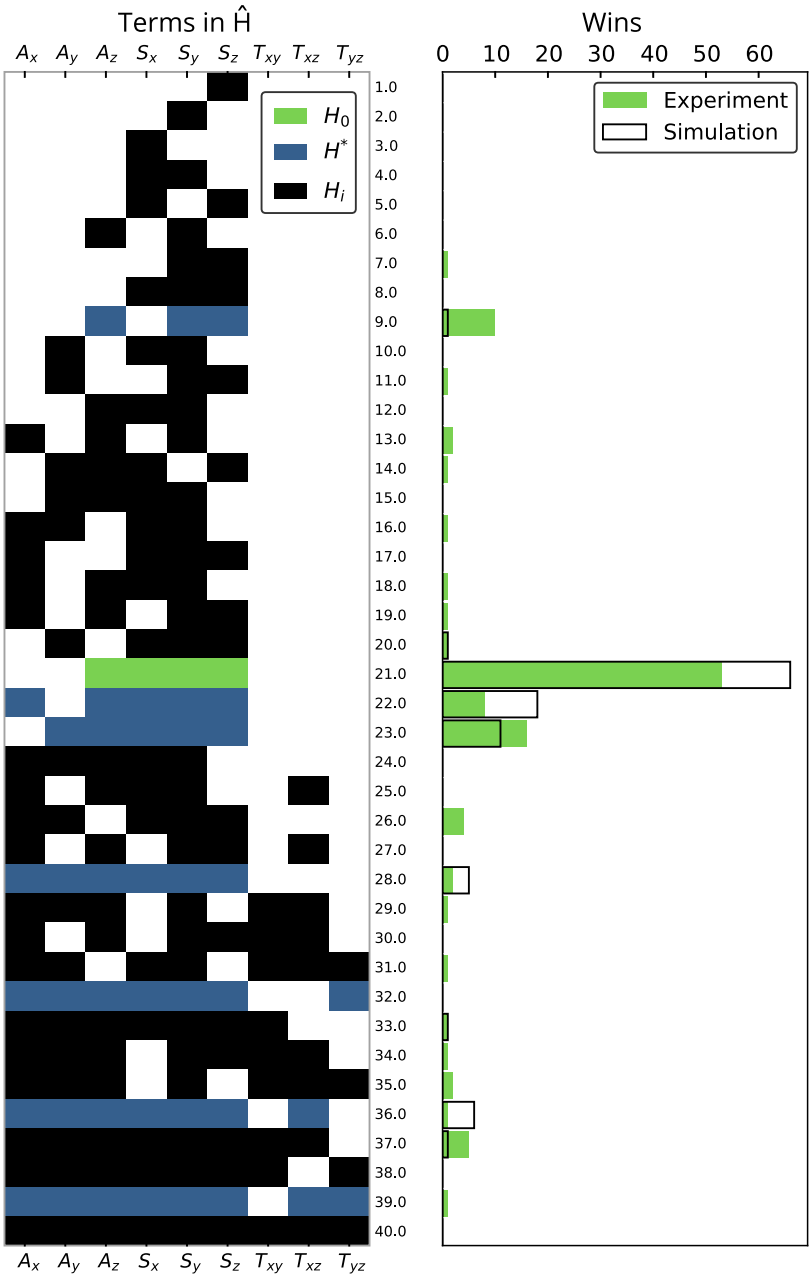

Figure 1.6: **Left,** map of the various Hamiltonian terms included in each of the possible 40 candidate models explored by QMLA during any of the 100 instances on either simulated or experimental data. IDs of candidate models are on the vertical axis, and labels for the terms on the horizontal axis. The true model $\hat{H}_0$ for the simulated case is highlighted in green and a subset of credible models in blue, i.e. models which may reasonbaly be expected to describe the targeted nitrogen-vacancy centre from theoretical arguments. **Right,** number of wins for each of the candidate models out of 100 independent QMLA runs. Cases adopting simulated data are shown by empty bars, with those using the experimental dataset shown by green bars. Implementation details are listed in **??**.

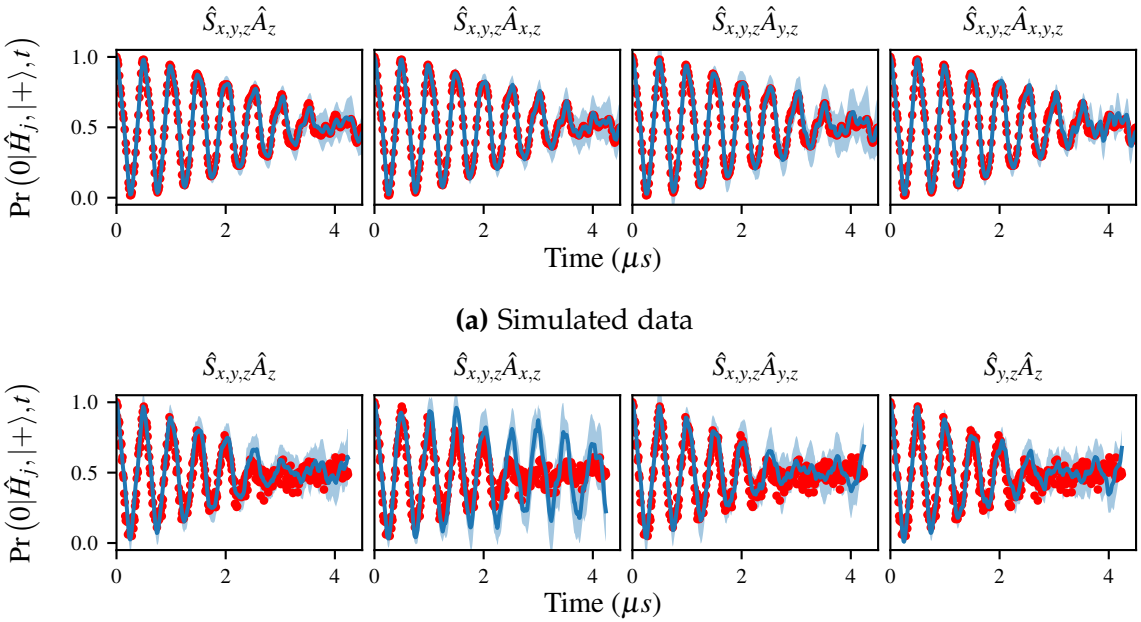

(a) Simulated data

(b) Experimental data

Figure 1.7: Dynamics reproduced by various QMLA champion models for **(a)** simulated and **(b)** experimental data. Likelihoods, $\Pr(0)$ are shown on y–axis with time on x–axis. Red dots give the true dynamics of $\hat{H}_0$, while the blue lines show the median reconstruction by $\hat{H}'$ from all the instances where that model was deemed $\hat{H}'$, with light blue showing the 67% confidence region. $\hat{H}'$ is listed on top of each plot; the number of instances won by each model can be read from Table 1.1. Implementation details are listed in **??**.

QMLA runs, as well as the win rate of each model. This ES is designed to study a small subspace of the overall available space: only 40 unique models are constructed. We highlight a number of *credible* models which we deem especially valid approximations of the target system, i.e. which contain the most viable approximations.

Fig. 1.7 shows the reproduction of dynamics of the top four models from both simulated and experimental runs. We see that each model faithfully captures the essential dynamics arising from the respective target systems; this alone is insufficient to conclude that the true model has been identified, but serves as a valuable *sanity-check*, convincing us that the output of QMLA is at least a sensible approximation of $\hat{H}_0$, if not the absolute true model.

The key insight promised by QMLA is to identfiy the interactions present in the studied system, which in this case was the decoherence processes of an NVC. In Fig. 1.8 we show the number of times each of the terms permitted, i.e. $\hat{t} \in \mathcal{T}_{\text{NV}}$ from Eq. (1.14), are included in the champion model, as well as the distribution of parameter estimates for those terms. From the simulated case, we see that those terms which are in $\hat{H}_0$, i.e. $\hat{t} \in \mathcal{T}_0$, are found in almost all instances. Furthermore, while most instances find a champion model which includes some

erroneous term(s), each $\hat{t} \notin \mathcal{T}_0$ is found with less than a quarter of the frequency of those $\hat{t} \in \mathcal{T}_0$. Hence terms outside of $\mathcal{T}_0$ may be reasonably ruled out in post-processing the QMLA results, by manually considering the relative frequency with which each term is found. The inaccurate terms found most often are seen to have (almost) negligible parameters: in conjunction with domain expertise, users can determine whether the inclusion of these terms are meaningful or simply artefacts of slight overfitting. In the experimental run, on the other hand, we see a similar gulf in frequency between some terms. Namely, $\{\hat{S}_x, \hat{S}_y, \hat{S}_z, \hat{A}_z\}$ are found in over 50 instances *more* than all other terms: we therefore conclude that those terms contribute most strongly to the NVC's decoherence process. The resultant model, $\hat{S}_{xyz}\hat{A}_z$ is in agreement with theoretical expectations, and shows that we can describe the intricate processes involved in decoherence through a relatively simple Hamiltonian, proving that QMLA can perform an important role in aiding the understanding of quantum systems.

1.5.2 *Finite size effects*

The case examined in this chapter is fundamentally limited by the nature of the approximation: by assigning a closed Hamiltonian to the NVC, we may never retrieve a complete description of the system. Closed, conservative dynamical systems – with a finite spectrum of permissible states – will return to their initial state after some finite time, according to the Poincaré recurrence theorem [18]. For quantum systems, then, the Poincaré recurrence times $\{t_R\}$ correspond to the times at which the *global* system's state, $|\psi_g\rangle$, returns to its starting state, $\left|\langle\psi_g(t_R)|\psi_g(0)\rangle\right|^2 \approx 1$ [15]. Such a system is therefore expected to exhibit *revivals*; in the context of quantum many-body systems, this is where the system *rephases* some time after it had dephased. These revivals are not necessarily physical, but rather an artefact of the approximation: realistic systems are seen to decohere completely after some decoherence time without revivals, i.e. *irreversible decoherence*. The Poincaré recurrence time scales polynomially with the number of degrees of freedom, n, within the closed system: $t_R \sim n!$. That is, even though the system of many interacting components *will* rephase, the time required to do so may be greater than the age of the universe [24]. Conversely, in our simplistic two-qubit model, the spectrum of eigenenergies is artifically restricted, and so revivals will appear unrealistically quickly.

Fig. 1.9 shows the predicted revivals of $\hat{H}' = \hat{S}_{x,y,z}\hat{A}_z$, the model found by QMLA to describe the NVC in the above analysis. The predicted revivals are unlikely to correspond to further experimental data; we can see intuitively that the system had decohered completely and irreversibly after 4.2 µs. When modelling such systems in practice, these revivals are often suppressed by a time-dependent damping $e^{-\Gamma t}$, with Γ determined phenomononoligcally, in order to yield the irreversible decoherence observed in real experimental systems, including the one used throughout this chapter. Here our aim was to model the interactions of the NVC spin with its nearest environmental qubit, which would be undermined by including such a drastic time-dependent effect: we omit this factor in this work, however it will prove important to account for this behaviour in future applications of QMLA to open systems.

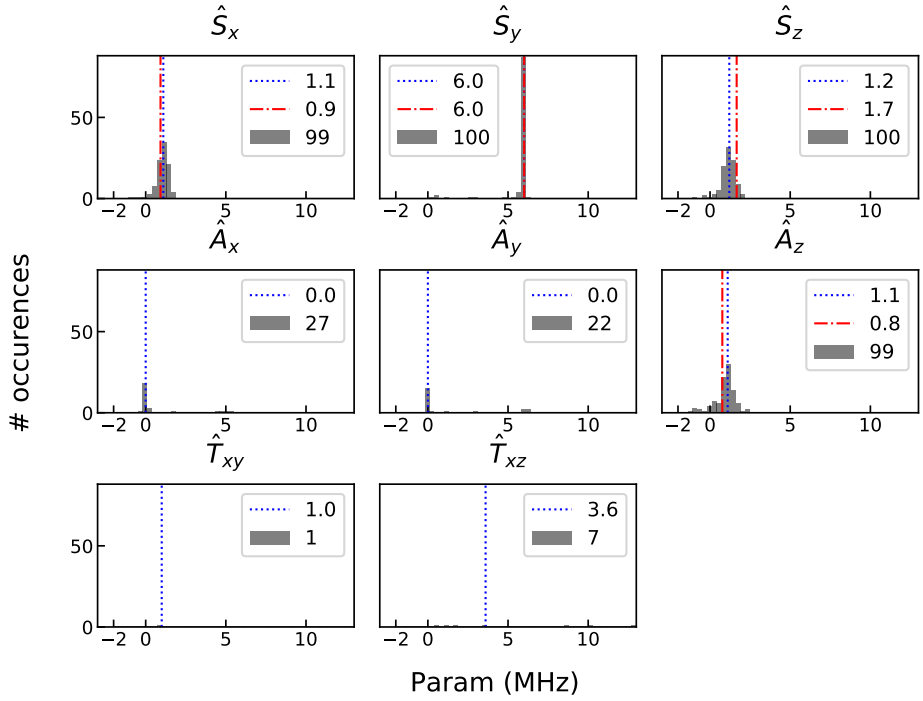

(a) Simluated QMLA instances. Red dotted lines show the true parameters.

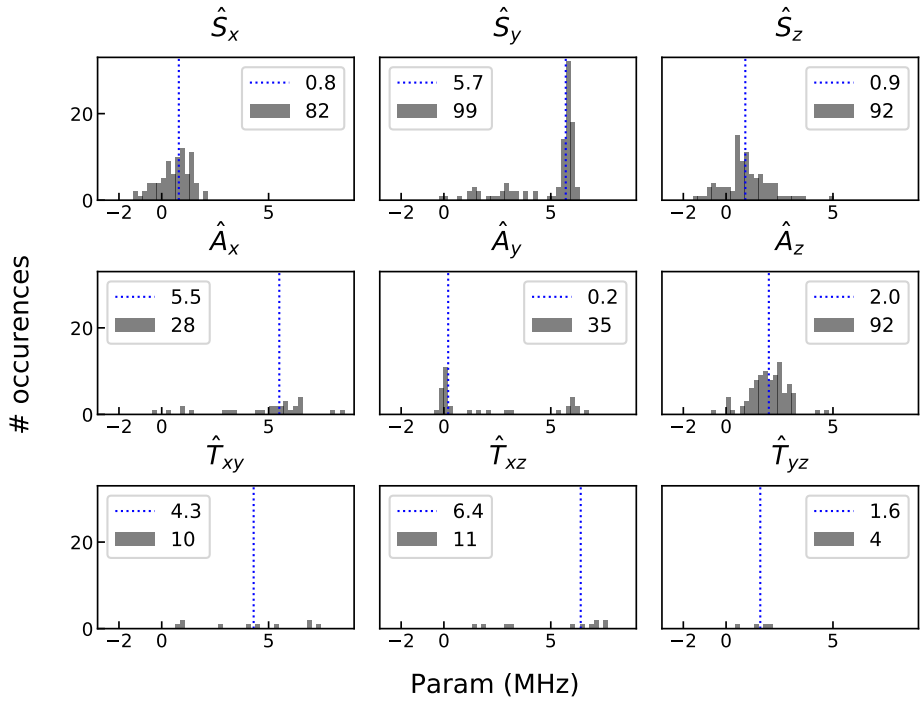

(b) Experimental QMLA instances.

Figure 1.8: Parameter values for terms found by QMLA. For each term found within the champion model of at least one instance of QMLA, a histogram is shown for the values of the term's associated parameter. The terms are listed along the top of each subplot with results for (**a**) simulated and (**b**) experimental data. Blue dotted lines indicate the median for that parameter, while red dotted lines give the true parameter in the simulated case. Grey blocks show the number of champion models which found the parameter to have that value, and the number listed in the legend reports the total number of champion models which contained that term. Implementation details are listed in **??**.

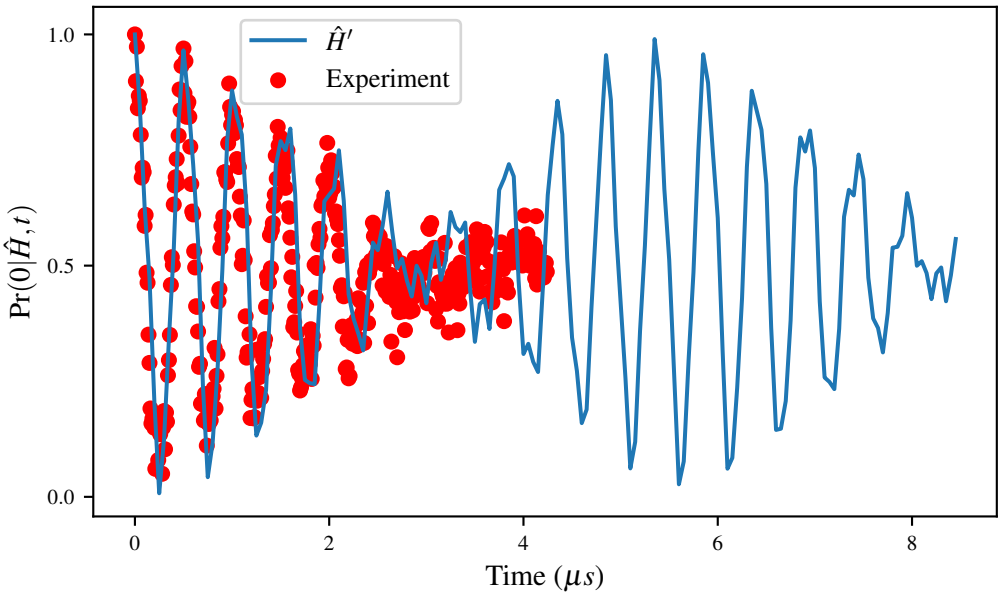

Figure 1.9: Predicted revivals of QMLA champion model, $\hat{H}'$ (blue), against the experimental data (red).

Invoking a finite-size bath to approximate the genuine open-system nature of the NVC permits us to examine the interaction of the spin with few neighbours, sufficient to characterise the domainant decoherence processes of a system, as we have done in this chapter. However, the approximation can not capture all of the spin's interactions, so we are motivated to consider models involving more nuclei, and ultimately models of open quantum system. In Chapter 2 we consider a similar NVC setup in simulation, to explore QMLA's capability while relaxing the effect of the finite size bath, and we note in Chapter 3 that in order for QMLA to prove useful in characterisation genuine quantum systems, we must incorporate complete open system models.

1.5.3 *Outlook*

We have thus characterised the interactions which dominate the decoherence process for a given NVC. In doing so, we identified not only the terms present, but also the strength (i.e. parameters) of those terms. Automated characterisation of quantum systems will be essential in the development of quantum technologies, whether for calibration of controlled devices, or alignment of experimental systems for optimal results. While this demonstration must be understood in the context of its limitations, e.g. the restricted basis studied, and the constrained model space searched, it represents a crucial proof of principle that QMLA is applicable to the task of automated quantum system characterisation. In the next chapter, we extend QMLA in simulation, to overcome some of the limitations mentioned here.

2 LARGER REALISTIC SYSTEMS

Chapter 1 concerned a two-qubit approximation of the short-time dynamics of an nitrogen-vacancy centre (NVC). It is valid criticism that the corresponding model space searched was reduced substantially through prior knowledge, and it therefore remains to test Quantum Model Learning Agent (QMLA) in a large model space, on physically meaningful data. In this chapter, we extend QMLA to consider appoximations of NVC sytems using more qubits, representing several nuclear sites, which aim to capture the interactions between the target NVC and the environment more thoroughly. Here we will simulate the target system, allowing us to make definite statements on the performance of QMLA, unlike the experimental data where we can not be sure of the dynamics' generator.

2.1 TARGET SYSTEM

A realistic model may be expected from considering the environment as a finite-size bath, consisting of n_s nuclear spins in addition to the NVC spin, i.e. the total number of qubits of such a model is $n_q = 1 + n_s$. The effects of nuclear spins are expected to manifest at higher times than those studied in Chapter 1, i.e. the decoherence of the NVC is only effected by the nuclear spins' independent precession at high times, so we must modify the experimental procedure accordingly. Such effects can also be highlighted by Hahn echo measurements, as in Fig. 1.2, except reversing the evoluting by $t' = t$ instead of $t' = 2t$ [12, 18], so our simulations will use this measurement scheme.

Since we are simulating the target system, we may choose the approximation we wish to invoke. Starting from the Hamiltonian expected to describe NVCs in [17], we again exclude the zero-field and quadrupole splitting (as in Eq. (1.4)), and assume the complete Hamiltonian to describe the long-time dynamics of an NVC,

$$\hat{H}_{\text{long}} = \mu_B g \mathbf{B} \cdot \mathbf{S} + \gamma \cdot \mathbf{B} \cdot \mathbf{I} + \mathbf{A} \cdot \mathbf{S} \cdot \mathbf{I}, \tag{2.1}$$

where[1]

- $\mu_B = 9.274 \times 10^{-24} \mathrm{J\,T^{-1}}$ is the Bohr magneton;
- $g \approx 2$ is the electron g-factor;
- $\mathbf{B}$ is the magnetic field with magnitude $B = 11\,\mathrm{mT}$;
- $\mathbf{S}$ is the total electron spin operator;
- $\mathbf{I}$ is the total nuclear spin operator.
- γ is gyromagnetic ratio, with dominant axial contributions from ^{13}C of $\gamma_z = 10.8\,\mathrm{MHz\,T^{-1}}$ and nonaxial contribution from proximal nuclei of $\gamma_x = \gamma_y = 42.6\,\mathrm{MHz\,T^{-1}}$ [25];

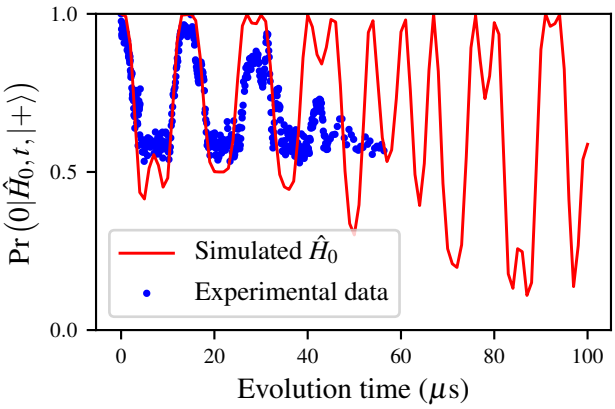

Figure 2.1: Long-time dynamics for nitrogen-vacancy centre, red, showing revivals, generated by $\hat{H}_0$ from Eq. (2.4), via Hahn echo measurement with $t' = t$. For comparison, experimentally generated dynamics are shown in blue.

- **A** is the hyperfine tensor, coupling the electron with the nuceli, here we take it to consist of $A = A_x = A_y = A_z = 0.2\,\text{MHz}$ [26].

We perform the same mapping to qubits as in Section 1.2: we let the first qubit represent the electron, and reduce the spin tensors to sums over nuclear sites, $\{\chi\}$. The complete model is then given by

$$\begin{aligned}\hat{H}_{\text{long}} =& \mu_B g B \sum_{w\in\{x,y,z\}} \hat{S}_w \\ &+ A \sum_{w\in\{x,y,z\}} \sum_{\chi\in\{\chi\}} \hat{S}_w \cdot \hat{A}_w^\chi \\ &+ B \sum_{w\in\{x,y,z\}} \gamma_w \sum_{\chi\in\{\chi\}} \hat{I}_w^\chi.\end{aligned} \tag{2.2}$$

For the purpose of testing QMLA, we can choose a subset of terms from Eq. (2.2) to consitute the true model: to set $\hat{H}_0$, we use the *secular* approximation, i.e. we assume the magnetic field is perfectly aligned along the z-axis [13]. In the secular approximation, the NVC spin qubit rotates only about the z-axis, and coupling between the NVC and nuclear qubits are only via $\hat{S}_z \cdot \hat{A}_z^\chi$. Here we will include the effect of the nuclear spins' rotations, which are much weaker and only

1 Note: the parameter values used here do not necessarily correspond to a physical system as they are taken from a range of sources. The precise values should not matter to the discussion, but are intended to generate dynamics using realistic values, which are similar to a genuine system, by inspection of Fig. 2.1.

Term	$\hat{t}$	Meaning	Parameter (Hz)	$\in \hat{H}_0$
$\hat{S}_x$	$\hat{\sigma}_x^1$	electron spin rotation about x-axis	2×10^9	No
$\hat{S}_y$	$\hat{\sigma}_y^1$	electron spin rotation about y-axis	2×10^9	No
$\hat{S}_z$	$\hat{\sigma}_z^1$	electron spin rotation about z-axis	2×10^9	Yes
$\hat{S}_x \cdot \hat{A}_x^j$	$\hat{\sigma}_x^1 \hat{\sigma}_x^j$	hyperfine coupling with j^{th} nuclear qubit, x-axis	0.2×10^6	No
$\hat{S}_y \cdot \hat{A}_y^j$	$\hat{\sigma}_y^1 \hat{\sigma}_y^j$	hyperfine coupling with j^{th} nuclear qubit, y-axis	0.2×10^6	No
$\hat{S}_z \cdot \hat{A}_z^j$	$\hat{\sigma}_z^1 \hat{\sigma}_z^j$	hyperfine coupling with j^{th} nuclear qubit, z-axis	0.2×10^6	Yes
$\hat{I}_x^j$	$\hat{\sigma}_x^j$	j^{th} nuclear spin rotation about x-axis	66×10^3	Yes
$\hat{I}_y^j$	$\hat{\sigma}_y^j$	j^{th} nuclear spin rotation about y-axis	66×10^3	Yes
$\hat{I}_z^j$	$\hat{\sigma}_z^j$	j^{th} nuclear spin rotation about z-axis	15×10^3	Yes

Table 2.1: Terms permitted in the QMLA GA (genetic algorithm) when in modelling the extended nitrogen-vacancy centre systems. Each term is permitted in the model search from expectations about the system under study. The succinct representaton is listsed as $\hat{t}$, along with an interpretation of the term's physical contribution to the system. The parameter values used in simulations can be found from from the listings of Eq. (2.1). The presence of the term in the true model is indicated in the final column: $\hat{t} \notin \hat{H}_0$ do not contribute to the dynamics of Fig. 2.1 but are available to the genetic algorithm (GA) when constructing models.

influence the NVC's decoherence at long times. In total then, the set of nuclear spins, $\{\chi\}$, are mapped to n_s qubits, and we define the true model as

$$\hat{H}_0 = \hat{S}_z + \sum_{j=2}^{n_q} \hat{S}_z \cdot \hat{A}_z^j + \sum_{w \in \{x,y,z\}} \sum_{j=2}^{n_q} \hat{I}_w^j, \tag{2.3}$$

with the parameters of Eq. (2.2) now absorbed, listed in Table 2.1, giving the dynamics in Fig. 2.1. For simplicity, we restate this in terms only of the Pauli matrices, where the first qubit refers to the NVC and the remaining qubits give the interactions and nuclear terms.

$$\hat{H}_0 = \hat{\sigma}_z^1 + \sum_{j=2}^{n_q} \hat{\sigma}_z^1 \hat{\sigma}_z^j + \sum_{w \in \{x,y,z\}} \sum_{j=2}^{n_q} \hat{\sigma}_w^j, \tag{2.4}$$

so in total, the set of terms for Q, $\mathcal{T}_0$, has 1 term for the NVC qubit, n_s terms for hyperfine couplings and $3n_s$ terms for the nuclei: $|\mathcal{T}_0| = 1 + 4n_s$.

We set the goal of QMLA as finding the approximation of Eq. (2.4), by allowing it to consider a wider set of terms. The permissible terms are then all terms from Eq. (2.2), i.e. the spin rotation terms about all axes, as well as all nuclei rotation terms, and the coupling terms:

$$\mathcal{T} = \left\{ \begin{array}{c} \hat{S}_w = \hat{\sigma}^1_w, \\ \hat{I}^j_w = \hat{\sigma}^j_w, \\ \hat{S}_w \cdot \hat{A}_w = \hat{\sigma}^1_w \hat{\sigma}^j_w \end{array} \right\} \tag{2.5}$$

for $w = \{x, y, z\}$ and $j \in \{2, ..., n'_q\}$. Note that n'_s is the number of nuclear spins considered by QMLA, but not necessarily the same number of nuclear spins, n_s, present in $\hat{H}_0$: in general $n'_s + 1 = n'_q \neq n_q$. In total, $|\mathcal{T}| = 3 + 3n'_s + 3n'_s = 3 + 6n'_s$.

Our aim is to test QMLA, so the choice of n_s and n'_s are arbitrary: we will allow QMLA to explore a larger model space than is required to capture the true model, in order to give QMLA the means to overfit as a robust test. For the target system we use $n_s = 3$ proximal spins, so that $|\mathcal{T}_0| = 13$; we allow candidates up to $n'_s = 5$, so $|\mathcal{T}| = 33$. In the most general sense, irrespective of the underlying physics we are simulating, here QMLA is aiming to identify the 13 terms truly present in Q, while searching the space of 33 permissible terms. Without imposing any restrictions on which combinations of terms are allowed, each term is simply either in $\hat{H}'$ or not, so can be thought of as binary variables: the total model space is therefore of size $2^{|\mathcal{T}|} = 2^{33} \approx 10^{10}$.

2.2 GENETIC ALGORITHM

GAs provide a robust and thoroughly tested paradigm for searching large candidate spaces; this is a natural framework through which we can explore such an unrestricted model space as described above. We have already extensively discussed the formalism of GAs in **??**, and specifically in the context of QMLA in **??**. Here we will use the same exploration strategy (ES) as described in **??**, i.e. where model generation is driven by a GA, and models are cast to chromosomes. In particular, candidate model's fitness will be computed from the residuals between their and the sytem's dynamics, described fully in **??**. This objective function (OF) relies on the definition of a validation dataset, $\mathcal{E}_v$, which we compose of tomographic probes (see **??**) and times generated uniformly up to $t_{max} = 100\mu s$, Fig. 2.2.

2.2.1 *Parameter learning*

Our primary goal in this chapter is to validate QMLA's performance in a very large model space, with over 10^{10} valid candidates. Our focus, then, is on model *generation*, and not concerned with parameter learning: we do *not* train models individually, but rather we assume access to a *perfect* parameter learning subroutine. That is, for each candidate, $\hat{H}_i$, considered, we simply assume knowledge of its parameters, $\vec{\alpha}_i$. This assumption is a major caveat to the results of this

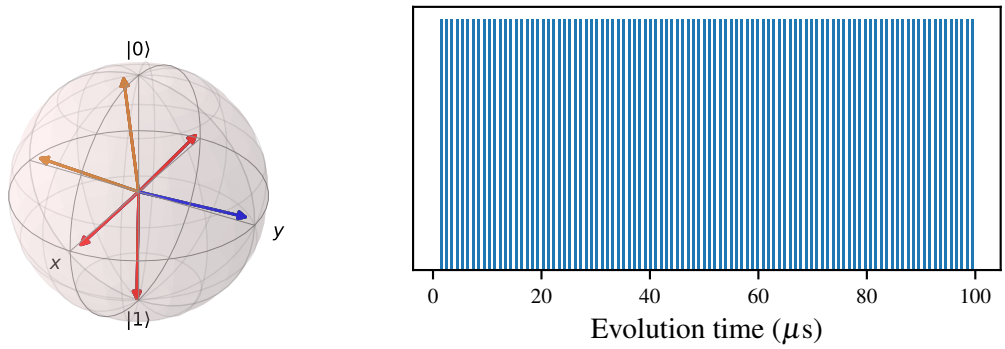

Figure 2.2: Evaluation dataset, $\mathcal{E}_v$, for nitrogen-vacancy centre genetic algorithm. **Left**, Set of probe states the NVC qubit is prepared in for evaluation, i.e. Ψ_v is close to the tomographic basis. Shown are the one-qubit probes on the Bloch sphere, which are combined to form n-qubit probes used when evaluating candidate models. **Right**, Time comb evaluated against, i.e. uniformly distributed times up to $t_{max} = 100\mu$s are used for experiments in $\mathcal{E}_v$.

chapter: no such perfect training scheme is known, so it remains to examine the detrimental effects of imprecisely finding $\vec{\alpha}_i' \approx \vec{\alpha}_i$. Moreover, while it is possible to extract information on the nuclear qubits from measuring only the NVC qubit, as in the Hahn echo measurements, it is uncertain whether any technique can simultaneously detect parameters of significantly varying orders of magnitude. For instance, some terms in Table 2.1 are $\mathcal{O}(\text{GHz})$, while others are $\mathcal{O}(\text{kHz})$; it is likely to prove difficult to discern the kHz parameters well, given that their contribution is equivalent to errors of order $\mathcal{O}(10^{-6})$ in the dominant GHz terms. Therefore we must caution that the results presented here, while demonstrating that QMLA *can* operate in large model spaces, are not immediately applicable to experimental systems, since there are outstanding challenges in the assessment of individual candidates, which must be overcome before the technique outlined can realistically succeed.

2.2.2 *Results*

At the instance level, we can see that the gene pool tends towards models of higher quality, captured[2] by their F_1-score, Fig. 2.3**(a)**. The improvement in modelling is reflected in the branch champions' predictive power at reproducing data generated by the system, Fig. 2.3**(b)**.

Considering the overall run, we see that QMLA is searching in a vast model space where randomly sampled models have poor F_1-score on average, Fig. 2.4**(a)**. QMLA efficiently explores the space by quickly moving into a subspace of high F_1-score, nominating $\hat{H}' = \hat{H}_0$ precisely in 85% of instances, Fig. 2.4**(b,c)**. The number of times each of the terms considered, Eq. (2.5),

2 The use of F_1-score as a figure of merit for candidate models in the QMLA search is described in **??**.

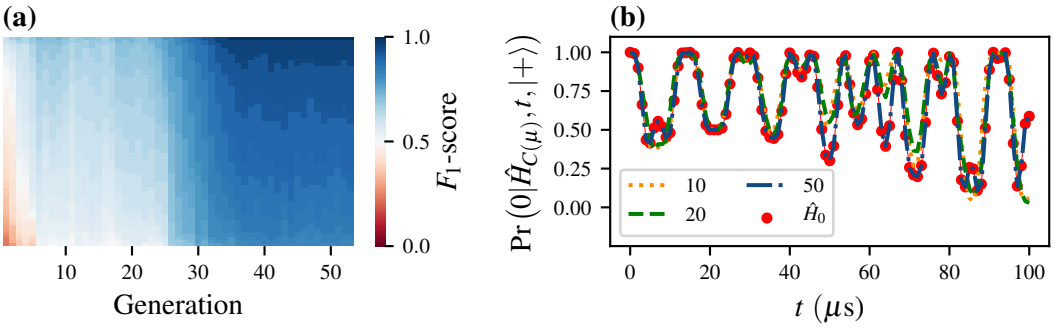

Figure 2.3: Instance of the genetic algorithm (GA) for simulated nitrogen-vacancy centre system with four qubits. **a**, Gene pool progression for the GA. Each tile represents a candidate model by its F_1-score. Each generation considers $N_m = 72$ models; the GA runs for $N_g = 53$ generations. **b**, Branch champions' dynamics. Each generation, μ, nominates a branch champion, $\hat{H}_{C(\mu)}$. Here, progressive generations' champions dynamics are shown against those of the target system, $\hat{H}_0$ (red).

are present in $\hat{H}'$ offers the most important insight from QMLA, namely the evidence in favour of each term's presence, which can be used to infer the most likely underlying physics. Here, $\hat{t} \in \mathcal{T}_0$ are found in $\geq 94\%$ of instances, while $\hat{t} \notin \mathcal{T}_0$ are found in $\leq 11\%$, shown in Fig. 2.5 and listed in Table 2.2. Such a discrepency, as well as the win rates for the models, allows for the clear declaration of the model $\hat{H}_0$ as the favoured representation for the quantum system.

By simulating a realistic system, we have hereby shown QMLA's ability to operate on physically meaningful data in large model spaces. The model search guided by a GA instructs QMLA to consider only ~ 1000 models out of the total space of $\sim 10^{10}$, clearly showing a drastic speedup in characterising Q when compared with brute force search. This demonstration is moderated by the presumptions which enabled us to perform simulations quickly and assume perfect outcomes from model training. However, taken together with the results of examining experimental data from Chapter 1, and the earlier confirmations of QMLA's operating principles in Part III, QMLA shows promise for characterising genuine small-to-medium quantum systems in the near future.

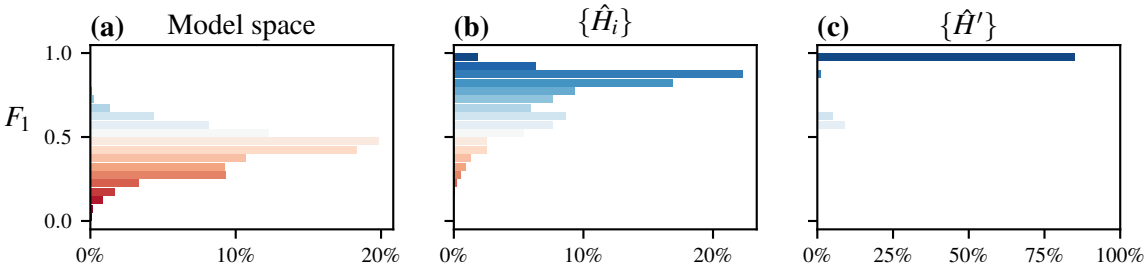

Figure 2.4: Nitrogen-vacancy centre genetic algorithm run. **a**, F_1-score of 10^6 samples from the model space of $2^{33} \approx 10^{10}$ candidate models, normally distributed around $f = 0.44 \pm 0.12$. **b**, The models explored during the model search of all instances combined, $\{\hat{H}_i\}$, show that QMLA tends towards stronger models overall, with $f = 0.79 \pm 0.16$ from $\sim 140,000$ chromosomes across the 100 instances, i.e. each instance tests ~ 1400 distinct models. **c**, Champion models from each instance, showing QMLA finds strong models in general, and in particular finds the true model ($\hat{H}_0$, with $f = 1$) in 85% of cases.

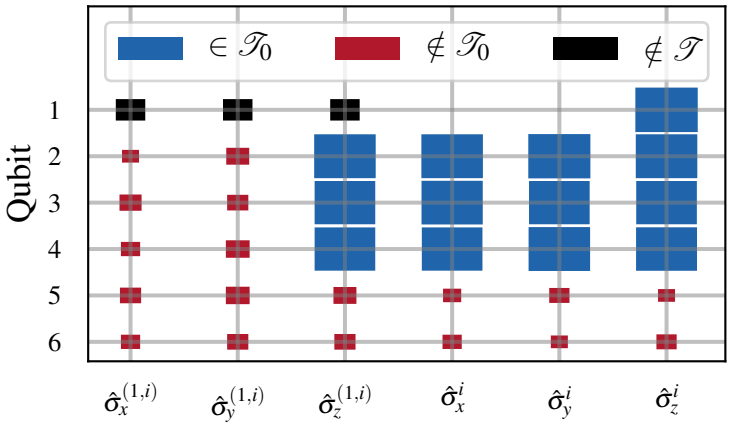

Figure 2.5: Hinton diagram of terms found for 4-qubit nitrogen-vacancy centre model. Terms are either in the target model ($\in \mathcal{T}_0$, blue) or not ($\notin \mathcal{T}_0$, red), or else not considered ($\notin \mathcal{T}$, black). Terms acting solely on the first qubit are the NVC spin's rotation terms, $\hat{\sigma}_w^1$, while each nuclear site also has rotation terms $\hat{\sigma}_w^j$. Hyperfine terms, $\hat{\sigma}_w^{(1,j)}$, couple the NVC qubit with the jth nuclear spin. The precise rate at which each term is detected can be read from Table 2.2.

Qubit	$\hat{\sigma}_x^{(1,i)}$	$\hat{\sigma}_y^{(1,i)}$	$\hat{\sigma}_z^{(1,i)}$	$\hat{\sigma}_x^{i}$	$\hat{\sigma}_y^{i}$	$\hat{\sigma}_z^{i}$
1	-	-	-	0	0	100
2	5	11	97	97	99	97
3	10	9	94	96	94	94
4	7	12	94	94	97	95
5	9	12	11	6	8	5
6	7	9	9	7	5	8

Table 2.2: Percentage of instances for which each term is found by QMLA GA studying NVC system.

Part V

CONCLUSION

3 OUTLOOK FOR MODEL LEARNING METHODOLOGIES

Optimal control techniques are a crucial component in improving quantum technologies, such that imperfect near-term devices may be leveraged to achieve some meaningful quantum advantages. The developments presented in this thesis contribute to the growing interest in automatic characterisation and verification of quantum systems and devices. Namely, the introduction of the Quantum Model Learning Agent (QMLA) represents an important advancement, whereby quantum systems can be completely characterised starting with little prior knowledge. The majority of this thesis was dedicated to the rigourous testing of QMLA, gradually moving from ideal scenarios in simulation to genuine experimental quantum systems.

We described the implementation of QMLA as an open source software platform in Part II, detailing numerous tunable aspects of the protocol, and their impact on training candidate models in **??**. QMLA facilitates customisation of its core elements and subroutines, such that it is applicable to a wide range of target quantum systems, as described in **??**–**??**. This malleability enables users to easily adapt the framework to their own needs, and formed the basis for the cases studied in the remainder of the thesis: we tested QMLA by devising a series of exploration strategies, each corresponding to a different target quantum system.

In Part III we considered ideal theoretical quantum systems in simulation. Initial tests in **??** showed that QMLA could distinguish between different physical scenarios and internal configurations. In **??**, we explored much larger model spaces by incorporating a genetic algorithm into QMLA's model design; the genetic algorithm showed promise for characterising complex quantum systems by successfully identifying the target model. The performance of the genetic algorithm, however, came at the expense of relying on a restrictive subroutine – used for training individual candidate models – drastically reducing its applicability to realistic systems. However, the restriction is permitted in the scope of characterising *controlled* quantum systems, for example new, untrusted quantum simulators.

We concluded the thesis by considering realistic quantum systems in Part IV. Experimental data from an electron spin in a nitrogen-vacancy centre was treated in Chapter 1; this too relied upon tailoring QMLA's procedure with respect to the system under study. A theoretically justified Hamiltonian is proposed by QMLA to describe the decoherence of the electron spin, yielding a highly predictive model in agreement with the system's measured dynamics, albeit exploring a small model space. To overcome concerns that the model search was artifically constrained in the context of realistic systems, Chapter 2 exercised QMLA in a vast model space, spanning terms which represent plausible interactions for the same type of system. Here, again, QMLA achieved high success rates, but with caveats on the subroutines assumed for model training, and resorting to simulated data.

In summary, this thesis has provided extensive tests of the QMLA algorithm, but each may be undermined by its individual constraints. In outlook, near-term developments of model learning methodologies in the context of quantum systems must address these shortcomings, for instance by unifying the strategies described in this thesis. Further, we anticipate immediate application in the study of open quantum systems, by replacing the Hamiltoinian formalism examined here with a Lindbladian representation, permitted within the QMLA apparatus. Through the advancements presented herein, we hope to have provided a solid foundation upon which these constraints may be relaxed, ultimately with a view to providing an automated platform for the complete characterisation of quantum systems. We envision QMLA as a straighforward but powerful utility for quantum engineers in the design of near term quantum devices, expecting continued development of the framework alongside the burgeoning open-source quantum software eco-system.

BIBLIOGRAPHY

[1] Antonio A. Gentile, Brian Flynn, Sebastian Knauer, Nathan Wiebe, Stefano Paesani, Christopher E. Granade, John G. Rarity, Raffaele Santagati, and Anthony Laing. Learning models of quantum systems from experiments, 2020. Accepted: Nature Physics.

[2] Brian Flynn, Antonio A. Gentile, Raffaele Santagati, Nathan Wiebe, and Anthony Laing. Quantum model learning agent: quantum systems' characterisation through machine learning. In preparation, 2021.

[3] Brian Flynn. Codebase: Quantum model learning agent. https://github.com/flynnbr11/QMLA, 2021.

[4] Quantum model learning agent documentation. https://quantum-model-learning-agent.readthedocs.io/en/latest/, Jan 2021. [Online; accessed 12. Jan. 2021].

[5] Marcus W Doherty, Neil B Manson, Paul Delaney, Fedor Jelezko, Jörg Wrachtrup, and Lloyd CL Hollenberg. The nitrogen-vacancy colour centre in diamond. *Physics Reports*, 528(1):1–45, 2013.

[6] Gordon Davies and MF Hamer. Optical studies of the 1.945 ev vibronic band in diamond. *Proceedings of the Royal Society of London. A. Mathematical and Physical Sciences*, 348(1653):285–298, 1976.

[7] J Meijer, B Burchard, M Domhan, C Wittmann, Torsten Gaebel, I Popa, F Jelezko, and J Wrachtrup. Generation of single color centers by focused nitrogen implantation. *Applied Physics Letters*, 87(26):261909, 2005.

[8] AM Edmonds, UFS D'Haenens-Johansson, RJ Cruddace, ME Newton, K-MC Fu, C Santori, RG Beausoleil, DJ Twitchen, and ML Markham. Production of oriented nitrogen-vacancy color centers in synthetic diamond. *Physical Review B*, 86(3):035201, 2012.

[9] A Lenef and SC Rand. Electronic structure of the n-v center in diamond: Theory. *Physical Review B*, 53(20):13441, 1996.

[10] Sebastian Knauer. *Photonic Structure Coupling and Strain Sensing with Single Photon Emitters*. PhD thesis, University of Bristol, 2016.

[11] MS Blok, Cristian Bonato, ML Markham, DJ Twitchen, VV Dobrovitski, and R Hanson. Manipulating a qubit through the backaction of sequential partial measurements and real-time feedback. *Nature Physics*, 10(3):189–193, 2014.

[12] L Childress, MV Gurudev Dutt, JM Taylor, AS Zibrov, F Jelezko, J Wrachtrup, PR Hemmer, and MD Lukin. Coherent dynamics of coupled electron and nuclear spin qubits in diamond. *Science*, 314(5797):281–285, 2006.

[13] L_G Rowan, EL Hahn, and WB Mims. Electron-spin-echo envelope modulation. *Physical Review*, 137(1A):A61, 1965.

[14] Forrest T Charnock and TA Kennedy. Combined optical and microwave approach for performing quantum spin operations on the nitrogen-vacancy center in diamond. *Physical Review B*, 64(4):041201, 2001.

[15] Antonio Andreas Gentile. *Operating practical quantum devices in the pre-threshold regime*. PhD thesis, University of Bristol, 2020.

[16] Lilian Isabel Childress. *Coherent manipulation of single quantum systems in the solid state*. Harvard University, 2007.

[17] Benjamin Smeltzer, Lilian Childress, and Adam Gali. 13c hyperfine interactions in the nitrogen-vacancy centre in diamond. *New Journal of Physics*, 13(2):025021, 2011.

[18] Heinz-Peter Breuer, Francesco Petruccione, et al. *The theory of open quantum systems*. Oxford University Press on Demand, 2002.

[19] Adam Gali, Maria Fyta, and Efthimios Kaxiras. Ab initio supercell calculations on nitrogen-vacancy center in diamond: Electronic structure and hyperfine tensors. *Physical Review B*, 77(15):155206, 2008.

[20] MV Gurudev Dutt, L Childress, L Jiang, E Togan, J Maze, F Jelezko, AS Zibrov, PR Hemmer, and MD Lukin. Quantum register based on individual electronic and nuclear spin qubits in diamond. *Science*, 316(5829):1312–1316, 2007.

[21] P-Y Hou, L He, F Wang, X-Z Huang, W-G Zhang, X-L Ouyang, X Wang, W-Q Lian, X-Y Chang, and L-M Duan. Experimental hamiltonian learning of an 11-qubit solid-state quantum spin register. *Chinese Physics Letters*, 36(10):100303, 2019.

[22] Stuart Russell and Peter Norvig. Artificial intelligence: a modern approach. 2002.

[23] David A Broadway, Jean-Philippe Tetienne, Alastair Stacey, James DA Wood, David A Simpson, Liam T Hall, and Lloyd CL Hollenberg. Quantum probe hyperpolarisation of molecular nuclear spins. *Nature communications*, 9(1):1–8, 2018.

[24] Maximilian Schlosshauer. Decoherence, the measurement problem, and interpretations of quantum mechanics. *Reviews of Modern physics*, 76(4):1267, 2005.

[25] Eugen Kubala, Kim A Muñoz-Álvarez, Geoffrey Topping, Christian Hundshammer, Benedikt Feuerecker, Pedro A Gómez, Giorgio Pariani, Franz Schilling, Steffen J Glaser, Rolf F Schulte, et al. Hyperpolarized 13c metabolic magnetic resonance spectroscopy and imaging. *Journal of visualized experiments: JoVE*, (118), 2016.

[26] S Felton, AM Edmonds, ME Newton, PM Martineau, D Fisher, DJ Twitchen, and JM Baker. Hyperfine interaction in the ground state of the negatively charged nitrogen vacancy center in diamond. *Physical Review B*, 79(7):075203, 2009.